2008-09

Comparison of linear and nonlinear processing with acoustic vector sensors

Psaras, Skevos T.

Monterey California. Naval Postgraduate School

NAVAL POSTGRADUATE SCHOOL

MONTEREY, CALIFORNIA

THESIS

COMPARISON OF LINEAR AND NONLINEAR PROCESSING WITH ACOUSTIC VECTOR SENSORS

by

Skevos T. Psaras

September 2008

Thesis Advisor:	Kevin B. Smith
Thesis Co-Advisor:	Joseph DiBiase

Approved for public release; distribution is unlimited

THIS PAGE INTENTIONALLY LEFT BLANK

REPORT DOCUMENTATION PAGE			Form Approved OMB No. 0704-0188
Public reporting burden for this collection of information is estimated to average 1 hour per response, including the time for reviewing instruction, searching existing data sources, gathering and maintaining the data needed, and completing and reviewing the collection of information. Send comments regarding this burden estimate or any other aspect of this collection of information, including suggestions for reducing this burden, to Washington headquarters Services, Directorate for Information Operations and Reports, 1215 Jefferson Davis Highway, Suite 1204, Arlington, VA 22202-4302, and to the Office of Management and Budget, Paperwork Reduction Project (0704-0188) Washington DC 20503.			
1. AGENCY USE ONLY ***(Leave blank)***	**2. REPORT DATE** September 2008	**3. REPORT TYPE AND DATES COVERED** Master's Thesis	
4. TITLE AND SUBTITLE Comparison of Linear and Nonlinear Processing with Acoustic Vector Sensors		**5. FUNDING NUMBERS**	
6. AUTHOR(S) LT Skevos Psaras			
7. PERFORMING ORGANIZATION NAME(S) AND ADDRESS(ES) Naval Postgraduate School Monterey, CA 93943-5000		**8. PERFORMING ORGANIZATION REPORT NUMBER**	
9. SPONSORING /MONITORING AGENCY NAME(S) AND ADDRESS(ES) N/A		**10. SPONSORING/MONITORING AGENCY REPORT NUMBER**	
11. SUPPLEMENTARY NOTES The views expressed in this thesis are those of the author and do not reflect the official policy or position of the Department of Defense or the U.S. Government.			
12a. DISTRIBUTION / AVAILABILITY STATEMENT Approved for public release; distribution is unlimited		**12b. DISTRIBUTION CODE**	

13. ABSTRACT (maximum 200 words)

Towed arrays of vector sensors are currently being employed in a variety of naval applications. The use of acoustic vector sensors, which measure the acoustic pressure and three orthogonal axes of associated particle motion, are of interest because of the signal gain and additional directionality achievable. The majority of analysis performed on vector sensor arrays has involved the advantages of conventional (linear) standard cardioid beamform processing. In this work, we shall explore the possible advantages of nonstandard linear processing techniques as well as new nonlinear (but non-adaptive) beamforming processors. The performance of these various beamforming methods will be examined using standard FFT processing of simulated data from a parabolic equation model in the band of 1250 - 1750 Hz, for both high and low SNR targets, in an isospeed profile shallow water environment.

14. SUBJECT TERMS Acoustic Vector Field, Acoustic Particle Velocity, Acoustic Vector Sensors, Linear Beamforming, Nonlinear Beamforming			**15. NUMBER OF PAGES** 92
			16. PRICE CODE
17. SECURITY CLASSIFICATION OF REPORT Unclassified	**18. SECURITY CLASSIFICATION OF THIS PAGE** Unclassified	**19. SECURITY CLASSIFICATION OF ABSTRACT** Unclassified	**20. LIMITATION OF ABSTRACT** UU

NSN 7540-01-280-5500 Standard Form 298 (Rev. 2-89)
Prescribed by ANSI Std. 239-18

THIS PAGE INTENTIONALLY LEFT BLANK

Approved for public release; distribution is unlimited

COMPARISON OF LINEAR AND NONLINEAR PROCESSING WITH ACOUSTIC VECTOR SENSORS

Skevos T. Psaras
Lieutenant, United States Navy
M.S., Carnegie Mellon University, 2000

Submitted in partial fulfillment of the
requirements for the degree of

MASTER OF SCIENCE IN APPLIED PHYSICS

from the

NAVAL POSTGRADUATE SCHOOL
September 2008

Author: LT Skevos T. Psaras

Approved by: Kevin B. Smith
Thesis Advisor

Joseph DiBiase
Thesis Co-Advisor

James Luscombe
Chairman, Department of Physics

THIS PAGE INTENTIONALLY LEFT BLANK

ABSTRACT

Towed arrays of vector sensors are currently being employed in a variety of naval applications. The use of acoustic vector sensors, which measure the acoustic pressure and three orthogonal axes of associated particle motion, are of interest because of the signal gain and additional directionality achievable. The majority of analysis performed on vector sensor arrays has involved the advantages of conventional (linear) standard cardioid beamform processing. In this work, we shall explore the possible advantages of nonstandard linear processing techniques as well as new nonlinear (but non-adaptive) beamforming processors. The performance of these various beamforming methods will be examined using standard FFT processing of simulated data from a parabolic equation model in the band of 1250 - 1750 Hz, for both high and low SNR targets, in an isospeed profile shallow water environment.

THIS PAGE INTENTIONALLY LEFT BLANK

TABLE OF CONTENTS

THIS PAGE INTENTIONALLY LEFT BLANK

LIST OF FIGURES

LIST OF TABLES

THIS PAGE INTENTIONALLY LEFT BLANK

I. INTRODUCTION

A great deal of work has been reported over the past decade on the processing of arrays of acoustic vector sensors [1], [2], [3], [4], [5], [6]. These sensors, which simultaneously respond to the scalar acoustic pressure and the vector motion of the medium (fluid velocity or acceleration), provide unique information on the total directional flow of acoustic energy at a single sensor. In this sense, each sensor independently provides three channels of directional sound signal information in addition to the standard pressure signal for an incident plane wave. Other work with vector sensors has concentrated on the theoretical development of processing techniques designed to combine these signals in a manner to best take advantage of their use [4], [5]. With the additional degrees of freedom available with four signal channels per sensor, there become a number of ways to combine the incoming signals and form a coherent beam pattern for both a single sensor as well as an array of such sensors. The most commonly studied has been the standard uniform cardioid beamform, associated with conventional linear vector sensor processing of equal pressure and vector velocity weighting, in which vector sensors have demonstrated a theoretical 6dB look direction signal gain over conventional linear scalar pressure arrays, in addition to impressive demonstrations of left/right ambiguity rejection not available to these arrays [4], [5].

Various, linear vector sensor weighting schemes have been evaluated in order to "optimize" the output of the beamformer in the context of maximizing directivity in the mainlobe while minimizing sidelobe interference [4]. Standard linear processing allows for ease of computation, using established Fast Fourier Transform (FFT) algorithms capable of "real time" implementation. These standard processing schemes, however, suffer from signal degradation in complex, interfering multi-path/multi-target environments. These efforts have led others to examine non-linear, data adaptive processing schemes that provide highly refined directivity in only the look direction [3], [7]. These processing schemes, however, in addition to the necessity for some degree of data conditioning, can become computationally cumbersome and thus best implemented in "post time" processing.

Still there exists the possibility for new processors, capable of providing better resolution in multi-path/multi-target arrival environments, but are non-adaptive, and capable of real time implementation using computationally efficient FFT algorithms. These processors range from uniquely weighted null-steered beams to nonlinear combinations of separately processed linear beamforms [8]. These processors may prove to have benefits in directivity and multi-target discrimination over the standard linear cardioid similar to the directivity increase already demonstrated over the conventional linear scalar pressure arrays.

Previous work by LT Eric P. Jautaikis of the Naval Postgraduate School demonstrates the advantages of vector sensor cardioid beamforming over conventional scalar pressure beamforming, in both look direction gain and ambiguous angle rejection, using a variety of processing techniques (including adaptive processing) and test case parameters [7]. The goal of this thesis it to expand on the results of this work in order to experiment with further gains and ambiguity rejection using the unique properties of pressure and vector velocity relative weighting in both linear and nonlinear (but non-adaptive) processing schemes developed by Professor Kevin B. Smith of the Naval Postgraduate School [8]. The benefit of these unique beamforming techniques over conventional cardioid beamforming will thus be explored using the same test case parameters developed by Jautaikis, with the benefit of the results of this work as a starting platform.

II. ACOUSTIC VECTOR FIELDS

The relationship between acoustic pressure and the acoustic particle velocity field provided by the Linear Euler Equation, as well as the assumptions provided by the Linear Wave Equation, provide both the fundamentals of signal propagation as well as the basis upon which the pressure and velocity signals can be combined in a coherent vector sensor beamforming algorithm [9], [10]. These relationships are critical to the Monterey-Miami Parabolic Equation (MMPE) propagation model used to generate the test data [11].

A. EQUATION OF CONTINUITY

Consider a volume element $dV = dxdydz$ in a fixed orientation in space. If we consider the rate of flow through the volume element in the x-direction, we get

$$\left[\rho v_x - \left(\rho v_x + \frac{\partial(\rho v_x)}{\partial x}dx\right)\right]dydz = -\frac{\partial(\rho v_x)}{\partial x}dV \tag{2.1}$$

where ρ is the fluid density. Doing the same for the other orthogonal directions generates a combined set of equations describing the net influx into volume element

$$-\left(\frac{\partial(\rho v_x)}{\partial x} + \frac{\partial(\rho v_y)}{\partial y} + \frac{\partial(\rho v_z)}{\partial z}\right)dV = -\nabla\bullet(\rho\vec{v})\,dV \tag{2.2}$$

The rate of mass increase in the volume element is given by

$$\frac{\partial m}{\partial t} = \frac{\partial \rho}{\partial t}dV\,. \tag{2.3}$$

Since the rate of increase of the mass must equal the net influx, combining Equations (2.3) and ((2.4)) yields the Mass Continuity Equation:

$$-\nabla\bullet(\rho\vec{v}) = \frac{\partial \rho}{\partial t} \tag{2.4}$$

B. EULER'S EQUATION

Next we consider the same fluid element, dV, but let this element move in space and allow it to contain a mass, dm, of the given fluid. By applying Newton's Second Law, the force exerted upon the mass of the element is

$$d\vec{f} = \vec{a}\ dm \tag{2.5}$$

As before, we consider the net force exerted upon the element in the x-direction

$$df_x = \left[P - \left(P + \frac{\partial P}{\partial x} dx \right) \right] dydz \ , \tag{2.6}$$

where P represents the total pressure. Similar equations can be found for the other orthogonal directions to give

$$d\vec{f} = -\nabla P dV \ . \tag{2.7}$$

The acceleration felt by the element can be shown to be

$$\vec{a} = \frac{\partial \vec{v}}{\partial t} + \frac{\partial x}{\partial t}\frac{\partial \vec{v}}{\partial x} + \frac{\partial y}{\partial t}\frac{\partial \vec{v}}{\partial y} + \frac{\partial z}{\partial t}\frac{\partial \vec{v}}{\partial z} \ , \tag{2.8}$$

which can be reduced to

$$\vec{a} = \frac{\partial \vec{v}}{\partial t} + \left(\vec{v} \bullet \nabla \right) \vec{v} \ . \tag{2.9}$$

We can now rewrite Newton's Second Law by combining Equations (2.6) and, (2.8) using the fact that the mass dm is equal to ρdV, as

$$-\nabla P = \rho \left(\frac{\partial \vec{v}}{\partial t} + \left(\vec{v} \bullet \nabla \right) \vec{v} \right) . \tag{2.10}$$

If we assume that the acoustic field represents a small perturbation to the ambient pressure and density of the medium, i.e.

$$P = P_0 + p' \ , \quad p \ll P_0 \ , \tag{2.11}$$

$$\rho = \rho_0 + \rho' \ , \quad \rho' \ll \rho_0 \, , \tag{2.12}$$

and the particle velocity is also a small quantity associated only with the acoustic field, then keeping just first order terms gives

$$\rho_0 \frac{\partial \vec{v}}{\partial t} = -\nabla p' \, . \tag{2.13}$$

This is the Linear Euler's Equation, which relates the time dependence of the acoustic velocity field to the gradient of the pressure for small amplitude pressure and density perturbations within a fluid.

C. LINEAR EQUATION OF STATE

In water, the Linear Equation of State, describing the relationship between density and pressure, can be described by a stress-strain curve, which can be described by the series expansion about the ambient pressure and density to 1st order as a linear approximation for small amplitude changes:

$$p' = \frac{1}{\rho_0} B\rho' = c^2 \rho' , \tag{2.14}$$

where $B = \rho_0 \frac{\partial P}{\partial \rho}$ represents the adiabatic bulk modulus and c represents the speed of sound in the fluid.

D. LINEAR WAVE EQUATION

We next wish to unify the Mass Continuity Equation and the Linear Euler's Equation. We begin by taking the divergence of the Linear Euler Equation (2.13)

$$\nabla \bullet \left(\rho_0 \frac{\partial \vec{v}}{\partial t} \right) = -\nabla^2 p' . \tag{2.15}$$

We then take the time derivative of the first-order terms in the Mass Continuity Equation (2.14) to obtain

$$-\nabla \bullet \left(\rho_0 \frac{\partial \vec{v}}{\partial t} \right) = \frac{\partial^2 \rho'}{\partial t^2} . \tag{2.16}$$

Combining these two equations with the Linear Equation of State (2.13) results in

$$\nabla^2 p' = \frac{\partial^2 \rho'}{\partial t^2} = \frac{1}{c^2} \frac{\partial^2 p'}{\partial t^2} , \tag{2.17}$$

This is the linear wave equation, and like the Linear Euler Equation from which it is derived, is valid for small amplitude pressure and density perturbations within a fluid.

E. PLANEWAVE PROPAGATION

The solution to the Linear Wave Equation (2.16) for a sound wave in the far-field can be approximated as a combination of planewaves of the form

$$p = Pe^{i(\vec{k} \bullet \vec{r} + \omega t)} , \tag{2.18}$$

where $\vec{k}$ is the angular wavenumber vector in the direction of the incoming wave at position $\vec{r}$, and ω is the angular frequency related by the relation $\omega = 2\pi f = ck$.

Similarly, by employing the Linear Euler Equation (2.12), we can describe the velocity field of an incoming planewave by

$$\vec{v} = \vec{V} e^{i(\vec{k}\bullet\vec{r}+\omega t)} \tag{2.19}$$

where the relationship between the magnitude of particle velocity and scalar pressure can be shown to be interchangeable by the "acoustic impedance" quantity, ρc, such that

$$V = \frac{P}{\rho c}. \tag{2.20}$$

The direction of $\vec{v}$ coincides with the direction of the wavenumber $\vec{k}$ .This then provides the basis for our vector geometry analysis, as both the pressure and velocity field are modeled as linear plane waves in the far field approximation.

F. VECTOR GEOMETRY

The use of vector data necessitates the establishment of a consistent geometry convention, visually illustrated below. The three vector components are aligned orthogonally along the x, y and z-axes, with the x-y plane defining the horizontal and the z-axis defining the vertical being positive downwards (as is typical in ocean acoustic models). Specific directions are then given by defining the x-axis along the $\theta = 0$ direction, the y-axis along the $\theta = 90°$, $\phi = 0$ direction, and the z-axis in the $\theta = 90°, \phi = 90°$ direction, as illustrated in Figure 1 below.

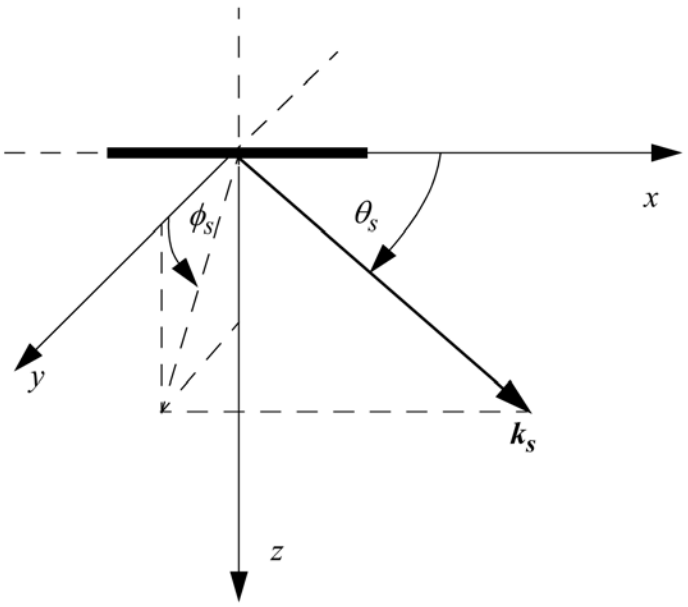

Figure 1. Vector Sensor Array Geometry

G. CARDIOID STEERING

To understand the response of an array of vector sensors, we begin by looking at the response of just a single vector sensor *m*. The plane wave response of each vector sensor velocity component is a dipole. We can write the general form of the time invariant vector sensor planewave response as

$$\vec{v}_m = \vec{V}_m e^{i\vec{k}\bullet\vec{r}_m}, \tag{2.21}$$

where $v_{xm} = V_{xm} e^{i\vec{k}\bullet\vec{r}_m}$, $v_{ym} = V_{ym} e^{i\vec{k}\bullet\vec{r}_m}$, and $v_{zm} = V_{zm} e^{i\vec{k}\bullet\vec{r}_m}$. Using the vector geometry defined, the response of each component is defined by

$$V_{xm} = V_m \cos\theta \quad , \quad V_{ym} = V_m \sin\theta\cos\phi \quad , \quad V_{zm} = V_m \sin\theta\sin\phi \ . \tag{2.22}$$

It is readily apparent that although velocity-only sensors have directivity gain over omni-directional pressure-only sensors, the velocity-only data produces no distinction between the mainlobe directivity response to an incident planewave and the equally directive backlobe. By combining the dipole velocity response with the omni-directional pressure signal, we are able to take advantage of the phase relationship

between the two to effectively "steer" a distinct mainlobe response for a single vector sensor. Figure 2 displays a single element vector sensor dipole response to a 1500 Hz planewave, scaled to a 40dB pressure magnitude reference for simplicity. These plots, and subsequent plots of this type, attempt to illustrate the nature of the response over all angles of θ and ϕ in the 3-D view (oriented for best null clarity), as well as the dominant null/mainlobe structure in the "cutaway" view along the plane of interest ($\phi = 0°$).

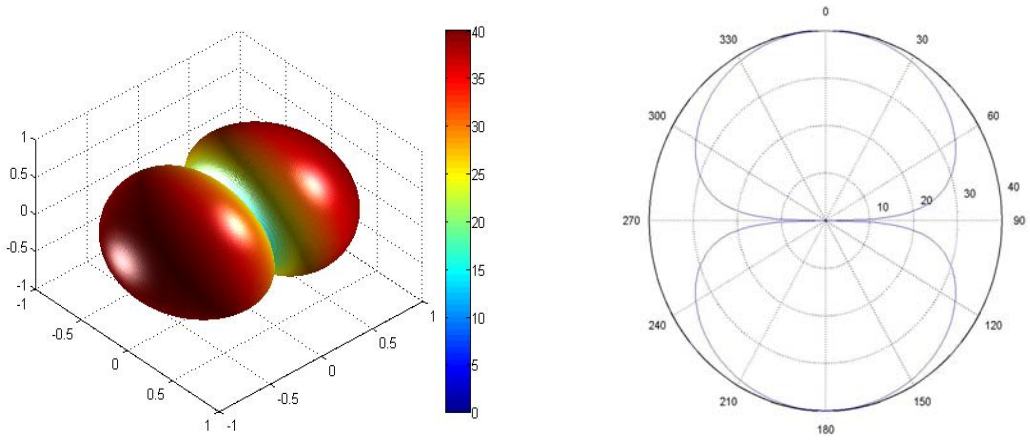

Figure 2. Single Element Velocity Dipole Response

In order to combine the omni-directional pressure and dipole velocity data, we simply re-scale either the pressure or velocity values relative to the other by the acoustic impedance, ρc, according to Equation (2.19) , e.g.

$$v_{pm} = V_{pm} e^{i\bar{k}\bullet\bar{r}_m}, \; V_{pm} = \frac{P_m}{\rho c} \; . \tag{2.23}$$

If we sum the weighted signals, pressure and three velocity components for our single vector sensor element, *m,* we can "steer" the response of the vector sensor, by

$$\begin{aligned} b_m\left(\theta_s, \phi_s\right) &= \left(w_{xm} v_{xm} + w_{ym} v_{ym} + w_{zm} v_{zm} + w_{pm} v_{pm}\right) \\ &= \left(w_{xm} V_{xm} + w_{ym} V_{ym} + w_{zm} V_{zm} + w_{pm} V_{pm}\right) e^{i\bar{k}\bullet\bar{r}_m} \end{aligned} \tag{2.24}$$

where $b_m(\theta_s, \phi_s)$ is the output from the combined signals and (θ_s, ϕ_s) represents the steering direction of the vector sensor. The weights applied to each component then dictate how the sensor is steered.

We then define the weights in terms of the dipole response of each vector sensor

$$w_{xm} = W_m \cos\theta_s,\ w_{ym} = W_m \sin\theta_s \cos\phi_s,\ w_{zm} = W_m \sin\theta_s \sin\phi_s, \text{ and } w_{pm} = W_m, \quad (2.25)$$

where W_m represents the scalar weighting value applied across the pressure and velocity channels. In this way, Equation (2.23) becomes an ideal "correlation" beamformer for a time invariant planewave, as we can vary the incident wave in all directions in θ and ϕ to produce a maximum response when $\theta_s = \theta, \phi_s = \phi$, or in the look direction defined by the "standard" convention of Equation (2.24). Applying this logic using "uniform" weighting of the single pressure and three velocity channels produces the standard cardioid response for a single, incident plane wave, as given by Figure 3.

It can be shown that when the sensor is properly steered in the same direction as the incoming plane wave, the standard uniform cardioid weighting summation reduces to

$$\begin{aligned} b_m(\theta_s = \theta, \phi_s = \phi) &= W_m V_m \left(\cos^2\theta_s + \sin^2\theta_s \cos^2\phi_s + \sin^2\theta_s \sin^2\phi_s + 1\right) e^{i\bar{k}\bullet\bar{r}_m} \\ &= 2W_m V_m e^{i\bar{k}\bullet\bar{r}_m} \end{aligned} . \quad (2.26)$$

This essentially produces twice the signal gain (6dB intensity) over the pressure-only sensor with the addition of the equally weighted dipole velocity component. This, however, is a measure of intensity directly at the look angle. When integrated over all θ and ϕ, the work of Cray and Nuttall (2001) demonstrates that the uniformly weighted cardioid sensor provides an overall increase of 3dB in directivity (intensity gain relative to an omni-directional pressure–sensor of equal power), in an isotropic noise environment [4]. In addition, unlike the pressure-only sensor, each element now becomes a uniquely "directional" sensor, with a broad mainlobe aligned in the steer direction, and a well-defined deep null in the direction opposite the incoming planewave [8].

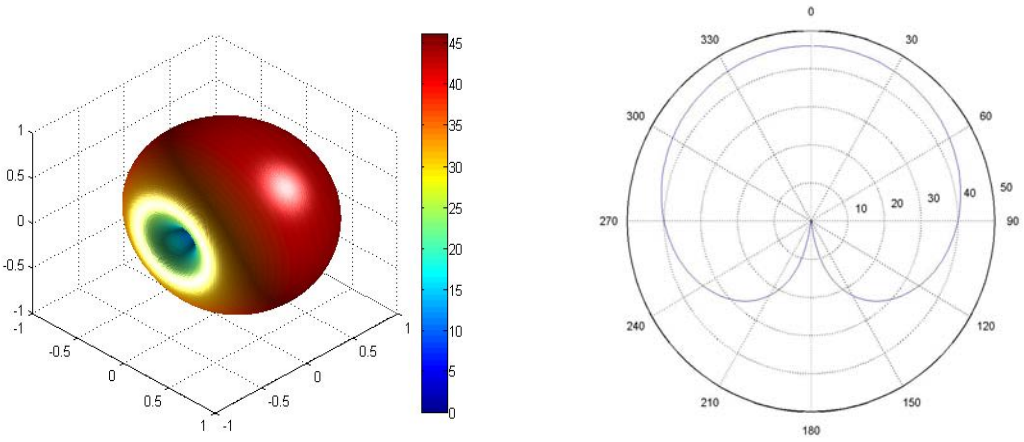

Figure 3. Single Element Cardioid Response

It can easily be shown that the relative pressure weighting determines the location of the null and the size of the lobes. This is apparent when the relative pressure weighting is decreased from unity (cardioid) to zero (dipole). In terms of a maximum sensor gain, a more "optimal" weighting can be defined by the relative scaling [4]

$$w_{xm} = 3W_m \cos\theta_s,\ w_{ym} = 3W_m \sin\theta_s \cos\phi_s,\ w_{zm} = 3W_m \sin\theta_s \sin\phi_s, \text{ and } w_{pm} = W_m. \quad (2.27)$$

This produces the plane wave response depicted in Figure 4. While this does provide an additional directivity in the steer direction, the deep null now occurs at ~110 deg relative to the mainlobe, and a distinct backlobe is now apparent opposite the steer angle.[8] Relative to the pressure-only case we find a vector sensor response of

$$\begin{aligned} b_m\left(\theta_s = \theta, \phi_s = \phi\right) &= W_m V_m \left(3\cos^2\theta_s + 3\sin^2\theta_s \cos^2\phi_s + 3\sin^2\theta_s \sin^2\phi_s + 1\right) e^{i\bar{k}\bullet\bar{r}_m} \\ &= 4W_m V_m e^{i\bar{k}\bullet\bar{r}_m} \end{aligned}, \quad (2.28)$$

or four-fold signal increase (12dB) in the look direction. This has been shown by Cray and Nuttall (2001) to provide the weighting of maximum (6dB) directivity gain in an isotropic noise environment, thus achieving the "optimal" weighting for peak array gain using standard linear processing techniques. [4] Caution should be used when applying weighting amplification, however, as this analysis does not take into account the increased channel noise that may result in low SNR environments, which will be significant later in this thesis.

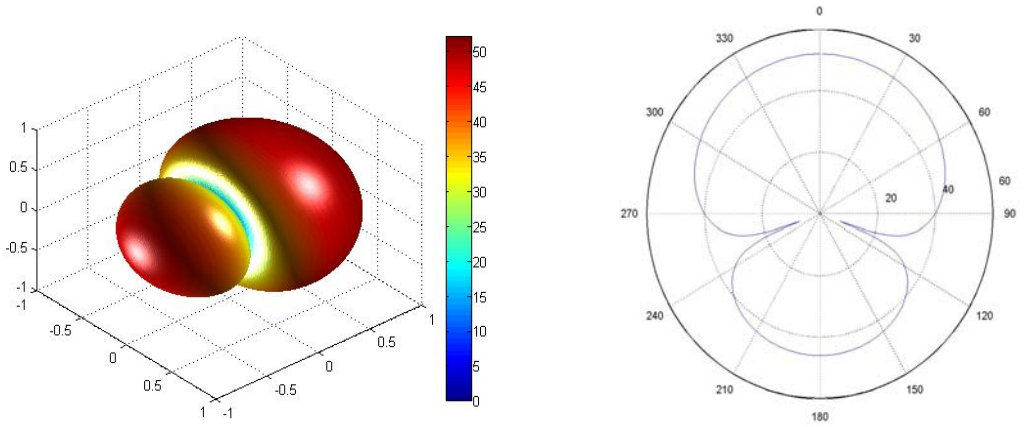

Figure 4. Single Element Optimal Response

This description of the optimal weighting scheme doesn't completely indicate how one may adjust the relative location of the null. Instead we introduce a general weighting scheme defined by [8]

$$w_{xm} = W_m \cos\theta_s \ , \ w_{ym} = W_m \sin\theta_s \cos\phi_s \ , \ w_{zm} = W_m \sin\theta_s \sin\phi_s \ , \text{ and } \ w_{pm} = AW_m$$

$$A = -\cos\left(\theta_0 - \theta_s\right). \tag{2.29}$$

where θ_0 represents the angle that we wish to steer the null. For example, to steer the null in the opposite direction from the mainlobe, we require $\theta_0 - \theta_s = \pi$ which leads to $A = 1$, or the standard cardioid pattern. Optimal weighting was achieved when we set $\theta_0 - \theta_s \approx 0.6\pi$ (or 110 deg), leading to $A = 1/3$. It can be shown that for any constant value of A the null is essentially "fixed" relative to the mainlobe, and the vector sensor steering pattern will have a planewave peak response when the steering direction aligns with the incoming signal, $\theta_s = \theta$.

To take this insight one step further, we may wish to effectively steer the null in the direction of the "ambiguous" or "conjugate" angle to the planewave arrival direction

θ relative to the "forward endfire" (θ = 0 °) x-axis of element orientation. In this case, we desire a null at the conjugate arrival path defined by $\theta_0 = 2\pi - \theta_s$, which by equation (2.28) is satisfied when [8]

$$A = -\cos\left(2\pi - 2\theta_s\right) = -\cos\left(2\theta_s\right) . \tag{2.30}$$

Caution must be used when applying this weighting scheme dynamically, however, as the peak response does not occur in the direction of the incoming signal as in the fixed case, but instead satisfies the equation [8]

$$\sin\left(\theta - \theta_s\right) = 2\sin\left(2\theta_s\right) . \tag{2.31}$$

If the incoming signal is along $\theta = 0$ or $\theta = \pi/2$, this equation may be solved analytically. In general, however, it is a transcendental equation. When $\theta = \pi/2$, the response can be shown to provide a peak at $\theta_s = \pi/2$ and a null in the ambiguous direction for all look angles, but produces a skew in peak response at other angles off broadside. Figure 5 displays the single element dynamic-null steering response for $\theta_s = \pi/2$ (broadside) and $\theta_s = \pi/4$ (45° from broadside), with θ_0 = 270° and θ_0 = 315° respectively. The mainlobe skew from the steer angle is most prominent for further off-broadside responses, however, the effect of this skew can be significantly reduced when multiple elements are combined coherently in array processing, as will be demonstrated later in this work. It can also be noted that unlike the previous single sensor weightings, which were "response insensitive" to orientation in θ and "structurally insensitive" along ϕ, dynamic null steering is "sensitive" to both. Thus we introduce a "forward endfire" axis for the dynamic null steered sensor (θ = 0°) along the x-axis. Although not instinctively evident from single element analysis, the greater significance of dynamic null placement along the conjugate arrival path θ_0 will have greater significance for our analysis of linear processing of an array of sensors along a common x-axis.

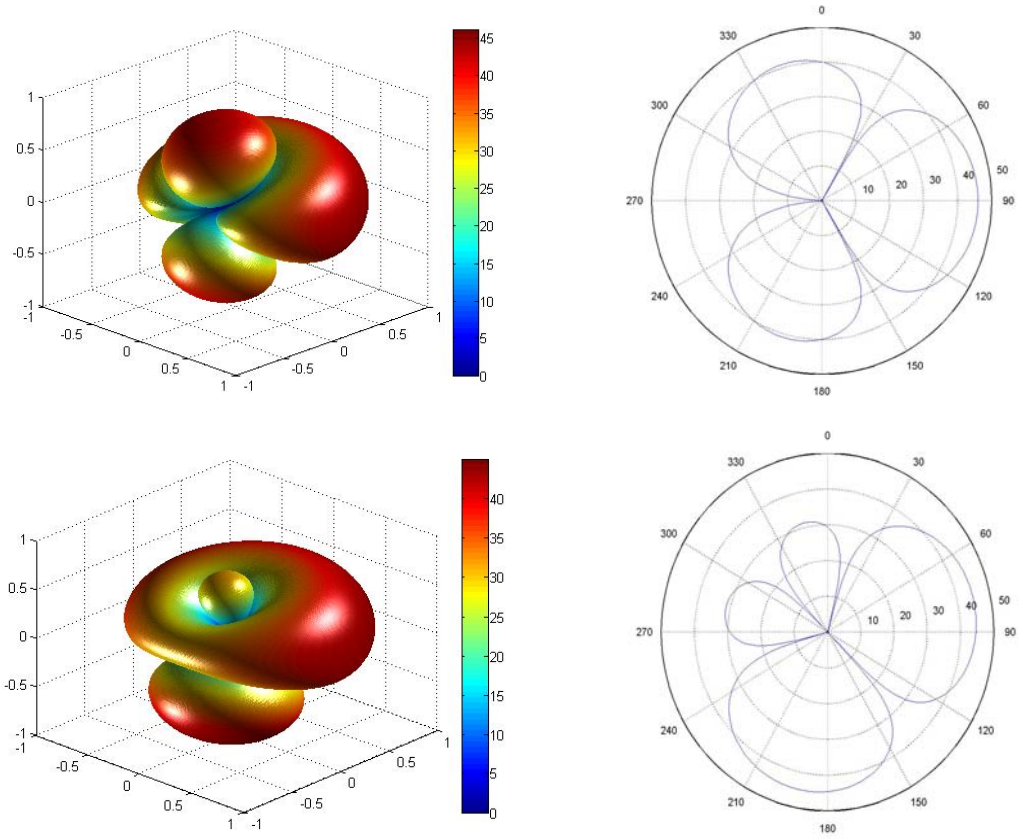

Figure 5. Dynamic Null-Steered Single Element Response at 90° (Top) and 45° (Bottom) Relative to Forward Endfire (Along the Vertical Axis)

H. LINEAR PROCESSING TECHNIQUES

For planewave beamforming, the time-invariant linear processor is typically defined by

$$B_{\textbf{linear}}^{(pv)}\left(\theta_s,\phi_s\right)=\left|\sum_m\left(w_{xm}v_{xm}+w_{ym}v_{ym}+w_{zm}v_{zm}+w_{pm}v_{pm}\right)e^{-i\vec{k}_s\bullet\vec{r}_m}\right|^2 , \qquad (2.32)$$

where $\vec{k}_s\bullet\vec{r}_n=kx_n\cos\theta_s$ indicates the steering direction of a linear array of elements oriented along the x-axis [4]. It is to be noted that, although individual elements can be steered independently in ϕ_s and θ_s, the array steering is only accomplished by relative

phases along the array axis, corresponding to steering in θ_s. Steering individual vector sensor elements independently is accomplished by adjusting the element weights independently as previously discussed. However, it is standard practice in linear processing to apply a common vector steering across the array, and will thus be the convention used throughout this thesis. This will have implications later when analyzing the result of applying fixed null weightings to individual elements in a linear array.

Linear array beamforming is based simply on matching the relative signal phases along the array as measured by each element. Like the ideal correlation processor for the single element weighting, the output of the beamformer is maximized when the steering direction, (θ_s, ϕ_s), matches the direction of the incoming planewave. Since $v_{xm} = V_{xm} e^{i\bar{k}\bullet\bar{r}_m}$, $v_{ym} = V_{ym} e^{i\bar{k}\bullet\bar{r}_m}$, $v_{zm} = V_{zm} e^{i\bar{k}\bullet\bar{r}_m}$ and $v_{pm} = V_{pm} e^{i\bar{k}\bullet\bar{r}_m}$, this can be further illustrated by rewriting Equation (2.32) as

$$B_{\mathbf{linear}}^{(pv)}(\theta_s, \phi_s) = \left| \sum_m \left(w_{xm} V_{xm} + w_{ym} V_{ym} + w_{zm} V_{zm} + w_{pm} V_{pm} \right) e^{i\left(\bar{k}\bullet\bar{r}_m - \bar{k}_s\bullet\bar{r}_m\right)} \right|^2 . \tag{2.33}$$

When $(\theta, \phi) = (\theta_s, \phi_s)$, Equation (2.33) shows that the phase mismatch term vanishes (i.e., $\vec{k} = \vec{k}_s$), and the array is properly steered for a peak response in the look direction. Equation (2.32) also provides an explanation of the inherent problem with conventional linear processing in regards to "left/right ambiguity". It can easily be shown that for pressure-only (scalar-pressure) beamforming, a peak response of equal magnitude will occur at both the look angle θ_s and it's conjugate angle $\theta_0 = 2\pi - \theta_s$ relative to the forward endfire axis, with no structural variation along ϕ. The addition of the vector data and weighting adds variation to ϕ, providing both directivity gain and left/right ambiguity "rejection". This will be illustrated in the subsequent sections.

In order to consider other vector sensor steering patterns, let us rewrite the steering of each element as

$$b_m^{(pv)}(\theta, \phi) = \left(w_{xm} V_{xm} + w_{ym} V_{ym} + w_{zm} V_{zm} + w_{pm} V_{pm} \right) e^{i\bar{k}\bullet\bar{r}_m} . \tag{2.34}$$

Note how this element steering maintains the relative signal phase along the array (defined by $\vec{k} \bullet \vec{r}_n$) and the term in parentheses has a maximum when $(\theta, \phi) = (\theta_s, \phi_s)$. Then

$$B_{\mathbf{linear}}^{(pv)}(\theta_s, \phi_s) = \left| \sum_m b_m^{(pv)}(\theta_s, \phi_s) e^{-i\vec{k}_s \bullet \vec{r}_m} \right|^2 . \tag{2.35}$$

Due to the linear nature of this processor, we could also write

$$B_{\mathbf{linear}}^{(pv)}(\theta_s, \phi_s) = \left| \sum_m b_m^{(p)} e^{-i\vec{k}_s \bullet \vec{r}_n} + \sum_m b_m^{(x)}(\phi_s) e^{-i\vec{k}_s \bullet \vec{r}_m} + \right.$$

$$\left. \sum_m b_m^{(y)}(\theta_s, \phi_s) e^{-i\vec{k}_s \bullet \vec{r}_m} + \sum_m b_m^{(z)}(\theta_s, \phi_s) e^{-i\vec{k}_s \bullet \vec{r}_m} \right|^2 , \tag{2.36}$$

where, for example, $b_m^{(x)}(\theta, \phi) = w_{xm} V_{xm} e^{i\vec{k} \bullet \vec{r}_m}$, and each vector sensor component is steered by the array phase (beamformed) before summing the components together. This form will be useful to consider in later algorithms [8].

In order to examine some fundamental responses of this linear processing approach, we consider a simple linear array of 256 elements with .25m element spacing, based on a ¼ wavelength (λ) spatial sampling for a 1500 Hz signal and a speed of sound (c) of 1500 m/s. The time-invariant reference planewave, incident in the horizontal ($\phi = 0$) at bearing angles on a both broadside (θ = 90°) and θ = 45° is linearly processed using the common vector steering scheme described by Equation (2.35), and applied to the variety of elemental weighting schemes already described for single element analysis. The inherent strengths and drawbacks of each weighting scheme are thus illustrated in terms of the benefit in both directivity and left/right ambiguity rejection over conventional scalar pressure arrays in Figures 6-9. These plots, again, are scaled relative to a 40 dB single element pressure magnitude response in order to demonstrate the expected array gain of the combined elements due to linear processing, as well as the azimuthul variation of the vector beamformers. They represent graphical mathematic

solutions to an “ideal” time-invariant planewave correlation processor “tuned” to a specific spatial wavelength in a perfectly noiseless environment, and are thus only valid for illustrative purposes.

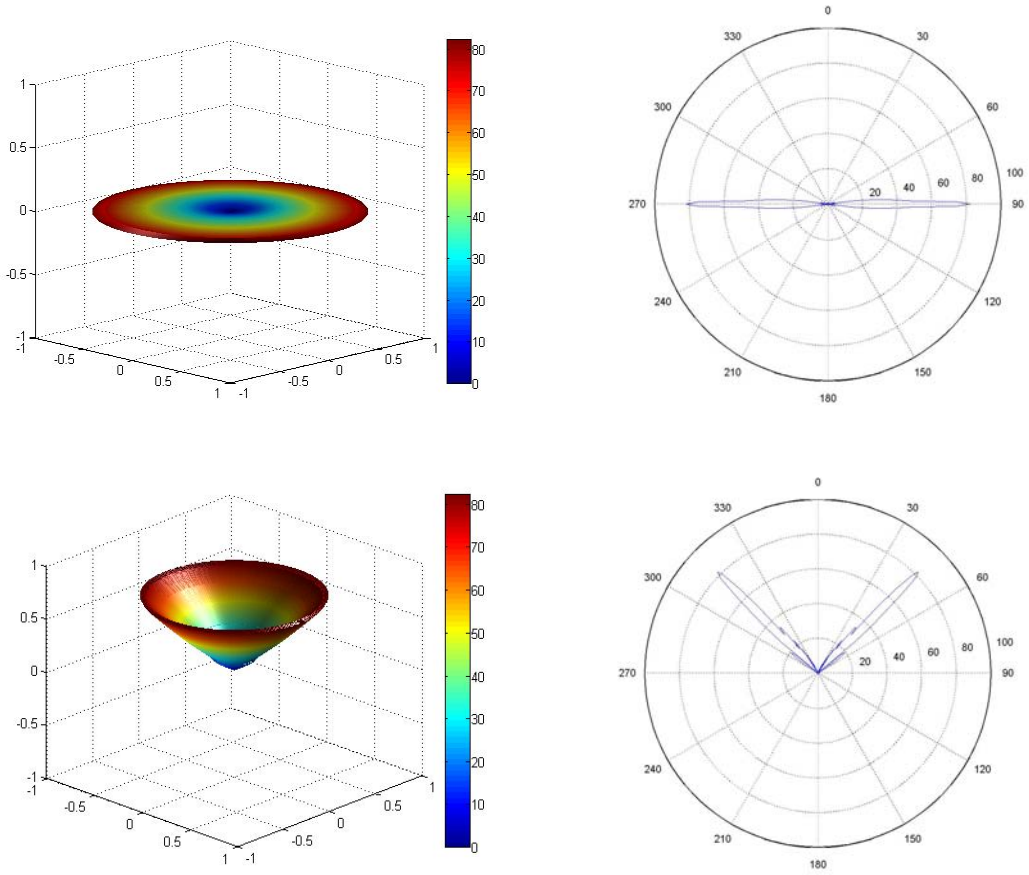

Figure 6. Scalar-Pressure Array Response at 90° (Broadside) and 45° Relative to Forward Endfire (Along the Vertical Axis)

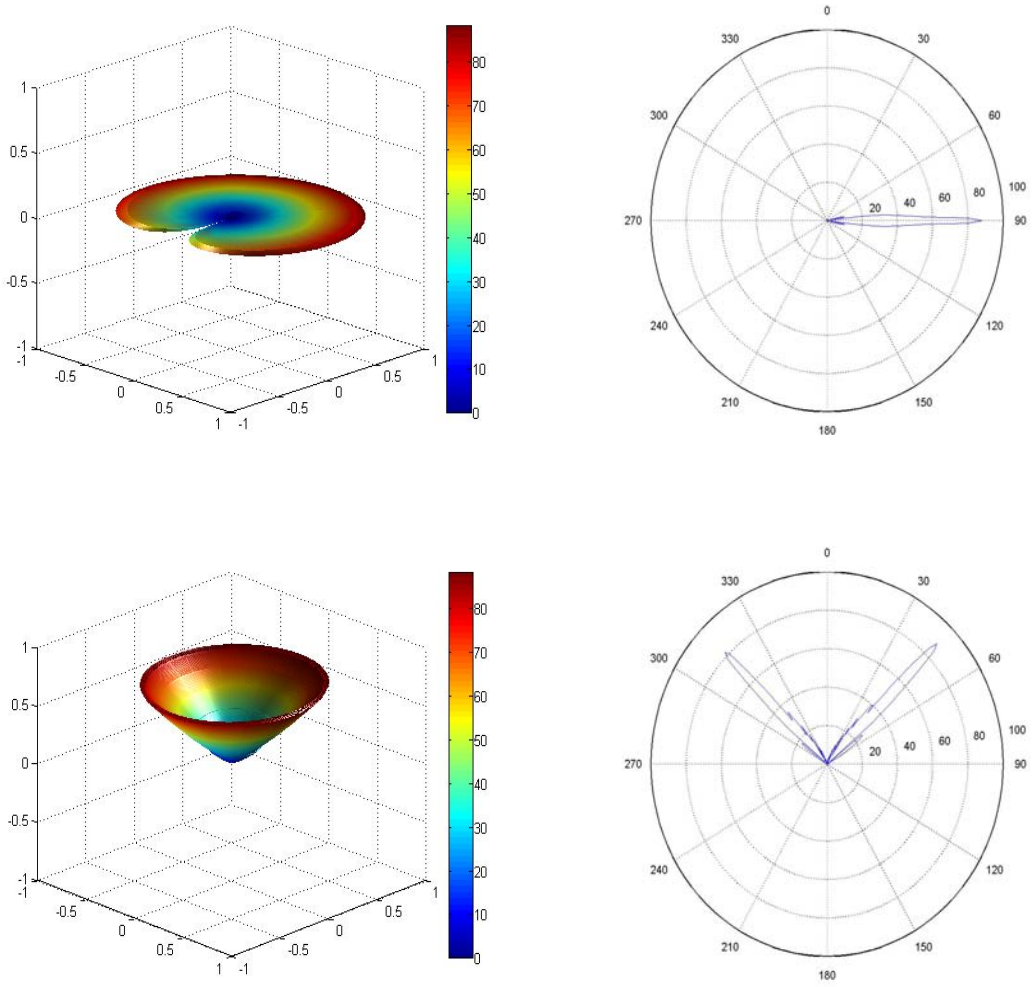

Figure 7. Uniformly Weighted Cardioid Array Response at 90° (Broadside) and 45° Relative to Forward Endfire (Along the Vertical Axis)

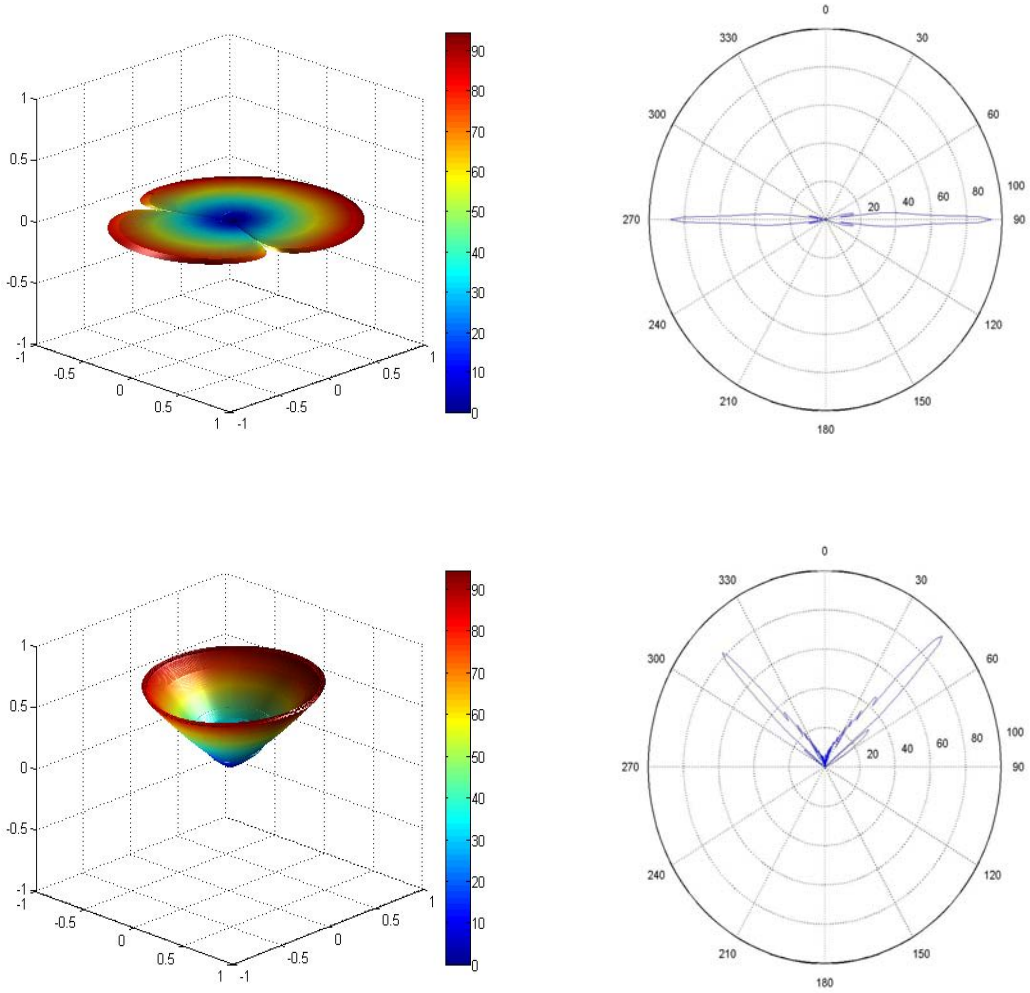

Figure 8. Optimally Weighted Array Response at 90° (Broadside) and 45° Relative to Forward Endfire (Along the Vertical Axis)

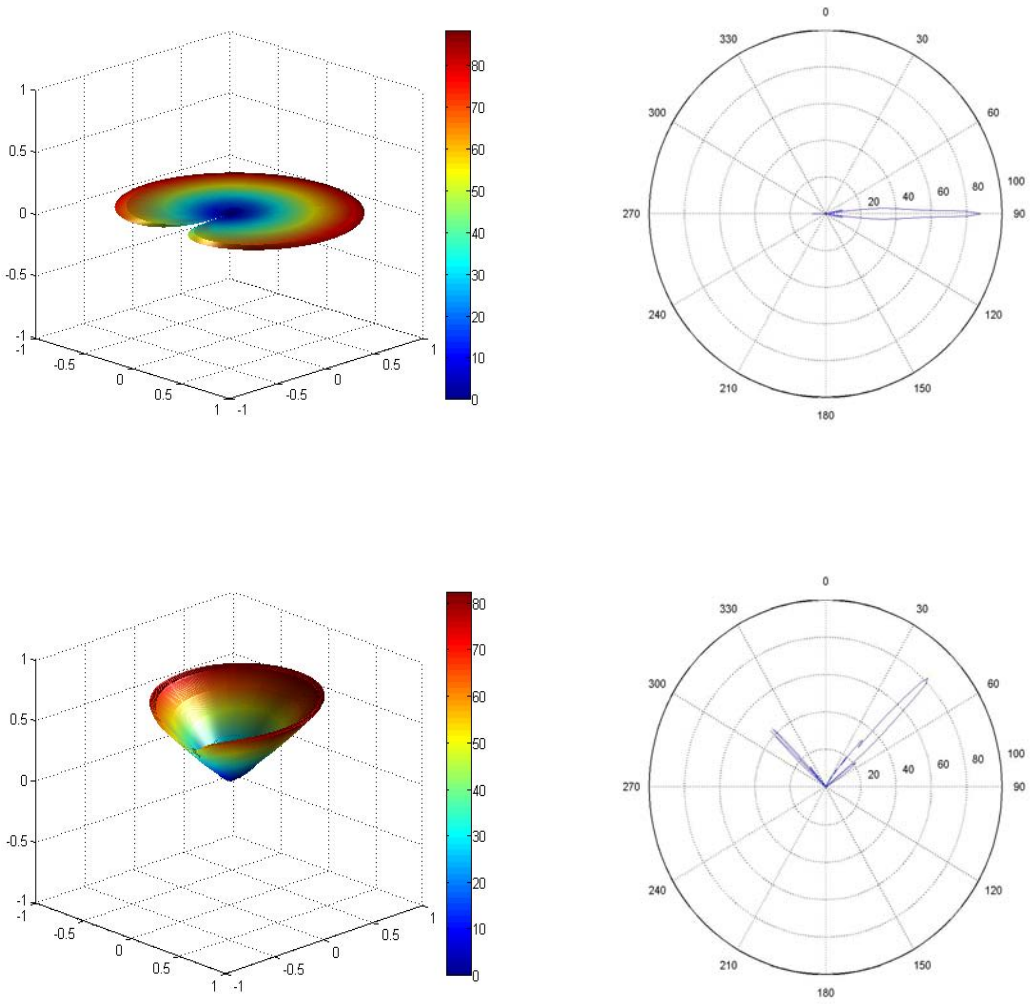

Figure 9. Null-Steered Array Response at 90° (Broadside) and 45° Relative to Forward Endfire (Along the Vertical Axis)

Initial observation from Figure 7 confirms that the uniformly weighted standard cardioid processor has directivity advantages at the broadside responses, yet falls short of left/right ambiguity rejection at the off-broadside angles. Figure 8 shows how the optimally weighted processor improves signal gain, but at the cost of left/right discrimination near broadside. This is an inherent drawback of a linear array of "fixed" null element weightings employing common vector steering, as the null of the individual

elements will not necessarily match with the conjugate look angle θ_0 This problem is alleviated by employing common dynamic null steering relative to forward endfire for the individual element weighting of the array. Figure 9 demonstrates that the null-steered processor shows good left/right discrimination in both the broadside and off-broadside cases. It can also be noted that although the dynamic null-steered processor sacrifices some gain in the look direction due to "skewing" of look angles for the individual elements, this is expected to be of little consequence for a sufficiently large number of array elements.

I. NON-LINEAR PROCESSING TECHNIQUES

The previous analysis of the linear beamformer discussed how different fixed null weightings show great directivity, but with some degradation in the processor's performance due to poor left/right ambiguity along some look directions. In contrast, the dynamic null-steered processor maintained positive ambiguity resolution, but at the cost of main lobe directivity at angles off broadside due to skewing. This leads us to consider some alternative techniques that attempt to combine the positive features from different linear processors in a non-linear fashion.

The different benefits of the cardioid and dynamic null-steering processors described earlier suggest a potential combination of the two outputs in a single processor. Specifically, we consider a new processor output defined by [8]

$$B^{(pv)}_{\textbf{cardynull}}\left(\theta_s,\phi_s\right)=\left|\sum_m b_m^{(pv)}\left(\theta_s,\phi_s\right)e^{-i\bar{k}_s\bullet\bar{r}_m}\right|\times\left|\sum_m b_m'^{(pv)}\left(\theta_s,\phi_s\right)e^{-i\bar{k}_s\bullet\bar{r}_m}\right| \tag{2.37}$$

where $b_m^{(pv)}\left(\theta_s,\phi_s\right)$ represents the standard cardioid weighting and $b_m'^{(pv)}\left(\theta_s,\phi_s\right)$ represents the dynamic null-steering with $A=-\cos\left(2\theta_s\right)$ [8]. This combined processor formulation will be referred to as "cardynull" processing. As can be readily seen in Figure 10, the high look direction gain of the cardioid and ambiguity rejection of null-steered weighting are retained in the ideal cardynull processor.

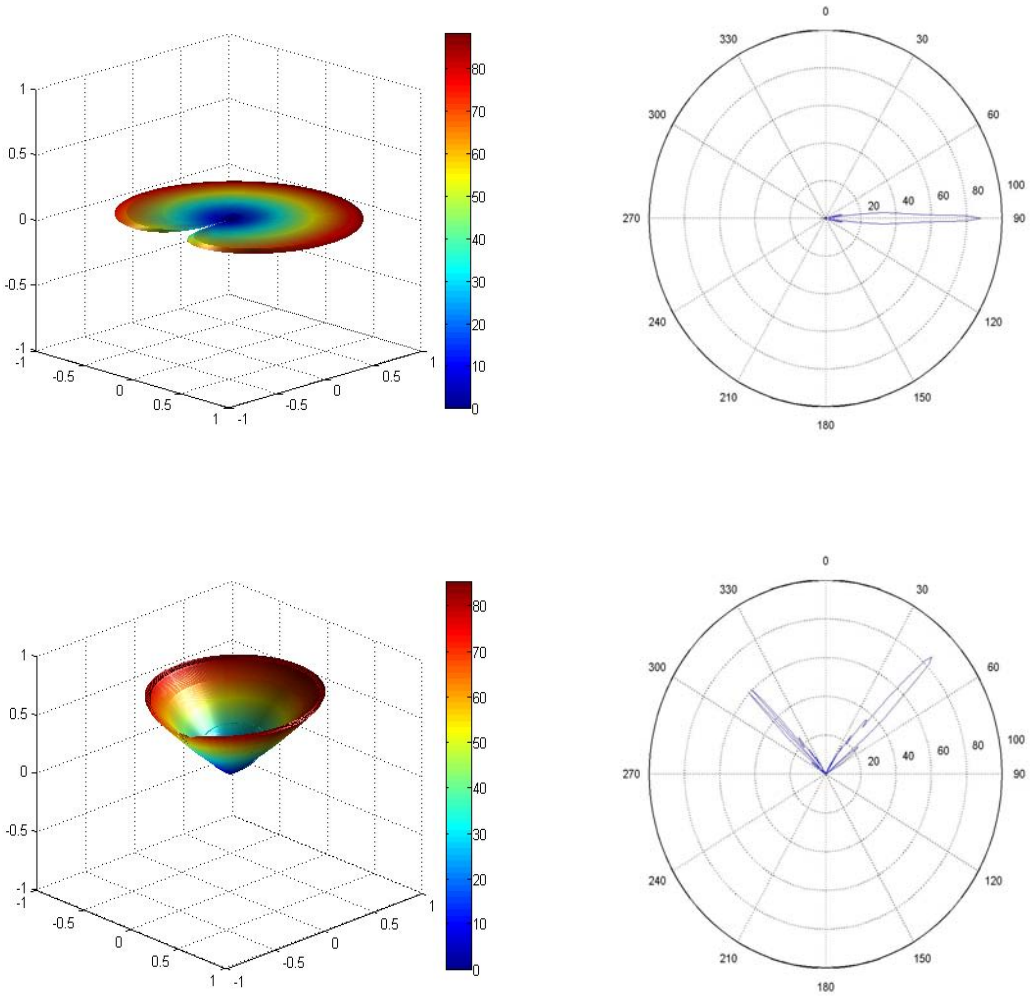

Figure 10. Cardynull Array Response at 90° (Broadside) and 45° Relative to Forward Endfire (Along the Vertical Axis)

Another approach to increase beam directivity would be to consider element steering patterns that reduce the width of the main lobe by expanding the region of the null. Motivated by the work of Smith and van Leijen [6], the non-linear "hippioid" results from the non-linear product of separately processed cardioid and velocity-only beamformers, such that

$$B^{(pv)}_{\textbf{non-linear-hippioid}}\left(\theta_s,\phi_s\right)=$$

$$\left|\sum_m b_m^{(p)} e^{-i\bar{k}_s\bullet\bar{r}_m}+\sum_m b_m^{(x)}\left(\phi_s\right)e^{-i\bar{k}_s\bullet\bar{r}_m}+\sum_m b_m^{(y)}\left(\theta_s,\phi_s\right)e^{-i\bar{k}_s\bullet\bar{r}_m}+\sum_m b_m^{(z)}\left(\theta_s,\phi_s\right)e^{-i\bar{k}_s\bullet\bar{r}_m}\right|\times$$

$$\left| \sum_m b_m^{(x)}(\phi_s) e^{-i\bar{k}_s \bullet \bar{r}_m} + \sum_m b_m^{(y)}(\theta_s, \phi_s) e^{-i\bar{k}_s \bullet \bar{r}_m} + \sum_m b_m^{(z)}(\theta_s, \phi_s) e^{-i\bar{k}_s \bullet \bar{r}_m} \right| , \qquad (2.38)$$

or simply

$$B^{(pv)}_{\textbf{non-linear-hippioid}}(\theta_s, \phi_s) = \left| \sum_m b_m^{(pv)}(\theta_s, \phi_s) e^{-i\bar{k}_s \bullet \bar{r}_m} \right| \times \left| \sum_m b_m'^{(pv)}(\theta_s, \phi_s) e^{-i\bar{k}_s \bullet \bar{r}_m} \right| , \qquad (2.39)$$

where $b_m^{(pv)}(\theta_s, \phi_s)$ represents the standard cardioid weighting and $b_m'^{(pv)}(\theta_s, \phi_s)$ represents the weighting with $A = 0$ (velocity-only dipole beamformer) [8].

As can be noted in Figure 11, the ideal hippioid processor produces similar left/right ambiguity rejection for signals arriving off-broadside as the cardynull processor. Near broadside, however, the hippioid performance still suffers from the lack of ambiguity rejection inherent in the velocity-only dipole component at these look directions. This is to be expected since the hippioid processor, like the other fixed null processors, simply narrows the main beam without affecting the steering of the null itself.

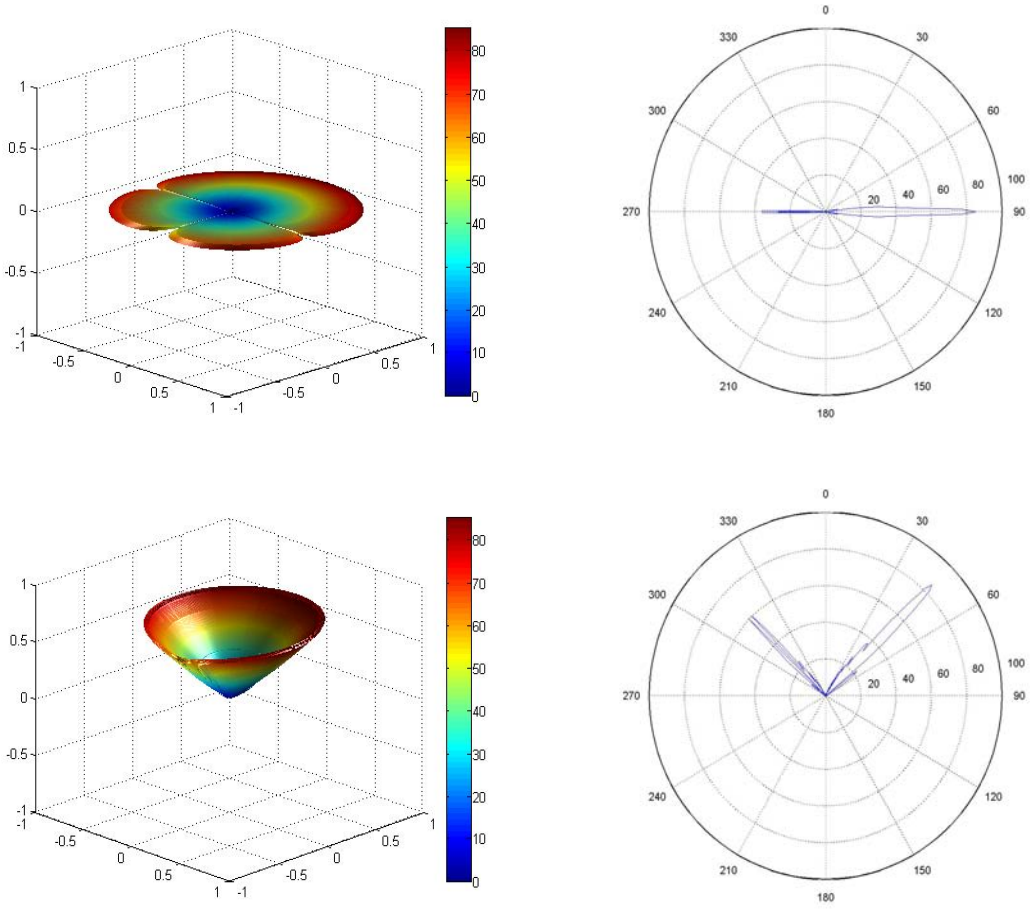

Figure 11. Hippioid Array Response at 90° (Broadside) and 45° Relative to Forward Endfire (Along the Vertical Axis)

THIS PAGE INTENTIONALLY LEFT BLANK

III. MONTEREY-MIAMI PARABOLIC EQUATION

The Monterey-Miami Parabolic Equation (MMPE) model [11], [12] is employed for the generation of all simulated ocean acoustic data in this thesis. This model, derived from the Helmholtz equation, utilizes the split-step Fourier (SSF) algorithm to generate stable, efficient solutions to the parabolic wave equation. Below is a description of the basic theory of the parabolic equation (PE), the split-step Fourier method used in the MMPE model, and the modifications and approximations used in generating the towed array data.

A. HELMHOLTZ EQUATION

To begin, we assume a time-harmonic acoustic field represented in cylindrical coordinates, i.e.

$$P(r,z,\varphi,\omega t) = p(r,z,\varphi)e^{-i\omega t}. \tag{3.1}$$

Substitution into the linear wave equation in cylindrical coordinates leads to the Helmholtz Equation,

$$\frac{1}{r}\frac{\partial}{\partial r}\left(r\frac{\partial p}{\partial r}\right)+\frac{1}{r^2}\frac{\partial^2 p}{\partial \varphi^2}+\frac{\partial^2 p}{\partial z^2}+k_0^2 n^2(r,z,\varphi)\,p = 0, \tag{3.2}$$

where $k_0 = \omega/c_0$ is the reference wave number, $n(r,z,\varphi) = c_0/c(r,z,\varphi)$ is the acoustic index of refraction, or the sound speed ratio between two mediums referenced to c_0. Thus all variations in the environment are represented within the function $n(r,z,\varphi)$.

B. PARABOLIC EQUATION APPROXIMATION

An approximation to the Helmholtz Equation begins by assuming cylindrical spreading in relation to a "reduced" pressure field defined by $u(r,z)$ such that

$$p(r,z) = \frac{1}{\sqrt{r}}u(r,z), \tag{3.3}$$

which, when substituted into Equation (3.2), yields

$$\frac{\partial^2 u}{\partial r^2}+\frac{1}{r^2}\frac{\partial^2 u}{\partial \varphi^2}+\frac{\partial^2 u}{\partial z^2}+k_0^2\left(n^2+\frac{1}{4k_0^2 r^2}\right)=0\,. \tag{3.4}$$

The last term drops off as $1/r^2$ and is generally ignored. Azimuthal coupling is introduced between radials by the second term, which is usually small and so typically neglected.

The remaining terms of the Helmholtz Equation can be factored after introducing an operator notation

$$P_{op}=\frac{\partial}{\partial r}, \tag{3.5}$$

$$Q_{op}=\sqrt{\mu+\varepsilon+1}\,, \tag{3.6}$$

where

$$\varepsilon=n^2+1\ , \tag{3.7}$$

$$\mu=\frac{1}{k_0^2}\frac{\partial^2}{\partial z^2}\ . \tag{3.8}$$

Proper factorization of the outward propagating field Ψ is obtained by defining

$$u(r,z)=Q_{op}{}^{-1/2}\Psi \tag{3.9}$$

The outgoing wave can then be represented by

$$P_{op}\Psi=ik_0 Q_{op}\Psi\,. \tag{3.10}$$

If we assume that backscatter is negligible, the complete description of the forward propagating acoustic energy is represented by Equation (3.10) and is the foundation for all underwater acoustic PE models.

If we assume a slowly-modulating function of the form $\Psi=\psi e^{ik_0 r}$, and rearrange Equation (3.10), we obtain

$$\frac{\partial\psi}{\partial r}=ik_0\left[Q_{op}-1\right]\psi \tag{3.11}$$

From this we define the parabolic approximation to the Helmholtz Equation as

$$\frac{\partial \psi}{\partial r} = -ik_0\left[1-Q_{op}\right]\psi = -ik_0 H_{op}\psi\,, \tag{3.12}$$

where $H_{op} = 1-Q_{op}$ represents the Hamiltonian-like operator defining the evolution of the PE field function in range, and the PE field function itself is defined by

$$p\left(\vec{r}\right) = P_0\sqrt{\frac{R_0}{r}Q_{op}{}^{-1/2}}\psi\left(\vec{r}\right)e^{ik_0 r}\,. \tag{3.13}$$

The vector $\vec{r}$ represents the vector notation from the origin to the point defined by $\left(r,z,\phi\right)$ in cylindrical coordinates.

To propagate the acoustic field, we depend on operations which can easily be performed using the SSF algorithm. To accomplish this, we employ the Thomson-Chapman wide-angle PE (TC-WAPE) operator splitting [15]

$$H_{op} = T_{op} + U_{op}\,, \tag{3.14}$$

where

$$T_{op} = 1-\left[1+\frac{1}{k_0^2}\frac{\partial^2}{\partial z^2}\right], \tag{3.15}$$

$$U_{op} = -\left(n-1\right)+U\left(\rho\right), \tag{3.16}$$

and $U\left(\rho\right)$ is defined to account for density contrasts at the water/bottom interface. By using the conventions

$$\psi\left(z\right) = FFT\left\{\hat{\psi}\left(k_z\right)\right\}, \tag{3.17}$$

$$\hat{\psi}\left(z\right) = IFFT\left\{\psi\left(k_z\right)\right\}, \tag{3.18}$$

we may write

$$T_{op}\left(\frac{\partial^2}{\partial z^2}\right)\psi\left(z\right) = FFT\left\{\hat{T}_{op}\left(-k_z^2\right)\bullet IFFT\left\{\psi\left(z\right)\right\}\right\}, \tag{3.19}$$

where we now have a scalar operator

$$\hat{T}_{op}\left(k_z^2\right) = 1-\sqrt{1-\left(\frac{k_z}{k_0}\right)^2}\,. \tag{3.20}$$

The PE field function is then marched forward in range by the SSF algorithm

$$\psi\left(r+\Delta r,z\right)=e^{-ik_0\frac{\Delta r}{2}U_{op}\left(r+\Delta r,z\right)}FFT\left\{e^{-ik_0\Delta r\hat{T}_{op}\left(k_z\right)}IFFT\left\{e^{-ik_0\frac{\Delta r}{2}U_{op}\left(r,z\right)}\psi\left(r,z\right)\right\}\right\}. \quad (3.21)$$

C. ACOUSTIC PARTICLE VELOCITY FIELDS

As previously shown by the linear Euler Equation (2.13), by taking the time derivative of the acoustic particle velocity and rearranging, the relationship between the time-harmonic acoustic pressure and particle velocity can be described as

$$\vec{v}=-\frac{i}{\omega\rho_o}\nabla p\,. \quad (3.22)$$

In cylindrical coordinates (ignoring azimuthal contributions), we can write Equation (3.22) as

$$\vec{v}=-\frac{1}{\omega\rho_o}\left(\frac{\partial}{\partial r}\hat{r}+\frac{\partial}{\partial z}\hat{z}\right)p\,. \quad (3.23)$$

By substitution of Equation (3.14), and employing the defining Parabolic Equation (3.13), the velocity components may be defined as

$$v_r\approx\frac{P_0}{c_0\rho_0}\sqrt{\frac{R_0}{r}}e^{ik_0r}Q_{op}\psi\ , \quad (3.24)$$

$$v_z=-\frac{iP_0}{\omega\rho_0}\sqrt{\frac{R_0}{r}}e^{ik_0r}\frac{\partial\psi}{\partial z}\ . \quad (3.25)$$

Each of these equations may be solved locally within the MMPE model. At each range step, the vector operation of Q_{op} defined by Equation (3.6) may be applied to Equation (3.21) to propagate the pressure field in the range direction. The vertical derivative in Equation (3.25) may also be solved by familiar Fourier transform techniques. Combined with the results of Equation (3.19), the final output of the MMPE model is then the complex pressure field and the radial and depth components of the complex velocity field. This approach has been shown to provide accurate solutions to the full vector field [12].

D. TOWED ARRAY APPROXIMATION

From the MMPE model, the acoustic pressure and particle velocity are calculated from the source location to a point specified by the first element of the array. The range step size for this part of the calculation is chosen to provide an accurate, long-range solution. After reaching the first element, the model adjusts the range step size to correspond to the separation between elements relative to the aspect angle of the array to the source. For example, using the geometry defined by Figure 1, if the element separation is designated d, then a source at end-fire will use a range step d to compute the propagation of the field from the first element to all subsequent elements, whereas for an arrival angle θ relative to forward end-fire, a range step of $d\cos\theta$ will be used. Thus, at broadside (θ = 90°), this reduces to a zero range step, and all elements record the same arrival structure in space [7]. This model assumes plane wave propagation from a far field source such that no significant curvature exists along the horizontal wavefront.

The MMPE model outputs the radial and depth components of velocity. Using our conventional geometry, the velocity response of each element in the x- and y-directions can be derived from the radial velocity component by

$$v_x = v_r \cos\theta \ , \ v_y = v_r \sin\theta \, , \tag{3.26}$$

where, again, θ represents the arrival angle measured from forward end-fire. The z-direction is then accounted for by the depth component of velocity v_z.

Using the results of the MMPE model, and the modifications to the radial component of acoustic particle velocity above, we now have the vector signal at each element of our array. By computing multiple frequencies over a specified bandwidth and employing standard broadband synthesis, acoustic time series can be generated. The output is then a set of matrices of elements versus time for pressure, and three components of acoustic particle velocity.

These simulate the received signal generated by a broadband source at a given range and environment along our towed array of 256 elements with .25 m spacing. For our broadband approximation, we set a 500 Hz filter band around our center frequency of

1500 Hz, such that the full frequency response of 1250Hz – 1750Hz (well within the spatial sampling constraints of our array spacing) is fully captured along the array aperture [7]. As most of our array processing assumes a far field planar wave response, a good approximation for the far-field (where wavefront curvature may be neglected) is provided when

$$r > \frac{\pi R^2}{\lambda} > 1.356R \tag{3.27}$$

where R is the maximum radial extent of the array [13]. Using 256 elements, with a spacing of 0.25m, results in a broadside far-field of approximately 6380 meters from the center of the array. This will be considered in choosing our test source ranges, and will be a significant factor for the response to a near field tow ship.

IV. DATA PROCESSING TECHNIQUES

In Chapter II, Equations (2.23) and (2.31) define the ideal correlation processor for both a single element and an array of elements respectively. In practice, it is a simple extension of these equations, when applied to the spectral content of the time-dependent data, that can be used to discretize a planewave response in both space (θ,ϕ) as well as time. This holds for all frequencies "tuned" to a minimum ½ wavelength distance between sampling point array elements, as long as the elements themselves sample the signal in time at the Nyquist rate of at least twice the incoming frequency [13]. These responses can then be correlated to the "replica" weights in order to maximize response along the look angle (θ_s,ϕ_s). Correlation processing can produce very accurate solutions to a time varying planewave response with respect to bearing resolution in the look direction. However, in practice this method can become computationally cumbersome in providing the exact, non-interpolated bearing solution needed to justify the added processing time [7]. Thus, for certain applications, where a higher level of resolution is not necessary, more "efficient" methods may be used to shorten the computational load.

A. FFT BEAMFORMING

FFT beamforming is a fast and efficient technique to linearly combine the data and compare it to a representative incoming plane wave. This method has been proven to be more efficient than plane-wave correlation processing due to existing optimized FFT algorithms in computational programs such as *Matlab*, but is generally not as accurate due to inherent interpolation necessary to quantify the spectral and spatial data [14]. These inaccuracies, however, have been shown to be of little consequence to the test cases provided [7].

1. Pressure-Only Processing

We begin with the time sampled pressure data, represented by a matrix $\boldsymbol{D}_p$, sampled over a given period, T. The data matrix can be decomposed into a compilation of data vectors, $\vec{d}$, such that

$$\boldsymbol{D}_p = \left[\vec{d}(0)\ \vec{d}(\Delta t)\, \vec{d}(2\Delta t) \ldots \vec{d}(T) \right], \tag{4.1}$$

which represents the data of every element at every time step. The vector $\vec{d}$ is made up of the pressure element level data received at a given instant in time from the first to last element. Thus the [*M*x*N*] data matrix has elements $D_{p(m,n)}$ that represent the measured pressure value at element *m* and sample time *n*, where M = 256 and N =512 in this analysis. The sampled data contains the desired pressure signal in the environment at the time of sampling for every array element. The MMPE model generates a coherent output data set, such that all frequency components within the signal are in phase at the source location. This is equivalent to transmission of an impulsive-like, coherent source. An example of the output data matrix for a single coherent source in an isospeed environment is shown in Figure 13. It represents the pressure output from the MMPE model on the towed array for a broadband (impulsive) source. As the signal passes across the array, we are able to determine the distinct characteristics of the wave, such as a strong received signal just after 3.3 seconds corresponding to the direct path signal, and multiple reflections off of the surface and bottom tapering in strength. A 100 dB dynamic range is used in order to fully illustrate the passing of the sound wave over the length of the array [7].

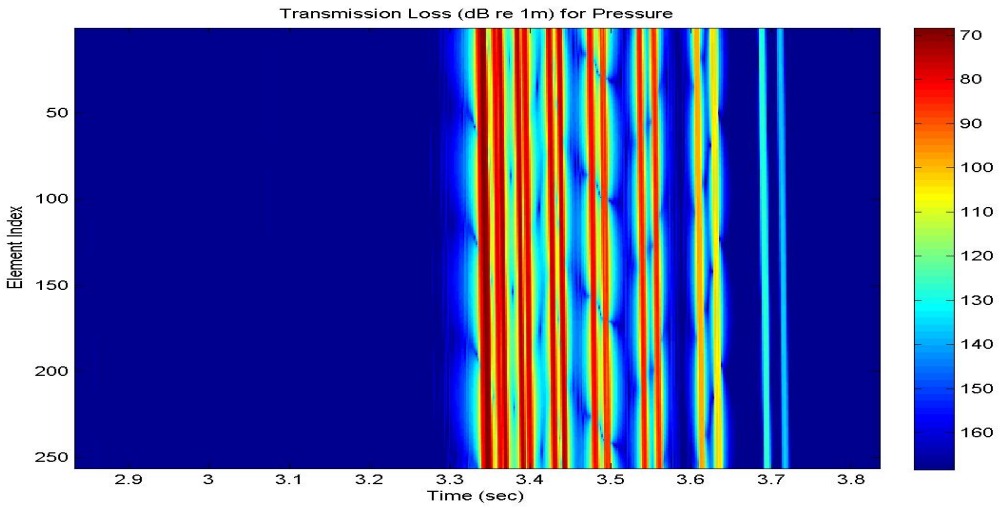

Figure 12. Time Sampled Data for Coherent Pressure Arrival Paths

Analysis of a coherent, impulsive source may have its advantages as far as illustration of the reinforcement of signal path along the frequency band. However, for the application of this thesis, we are interested in simulating a continuous signal in time. In order to simulate a continuous signal, we assume an incoherent source across the frequency band, such as would be realistic for a long duration source separated by an appreciable range. To allow for an incoherent source, every frequency bin of the signal was given a separate random phase factor of the form $e^{i2\pi\theta'}$, where θ' is a random number drawn from a uniform distribution over 0 to 1. When the random number is applied to our random phase factor, we generate a set of uniformly distributed random phase factors from 0 to 2π. An example of the output data matrix for an incoherent source is shown in Figure 13.

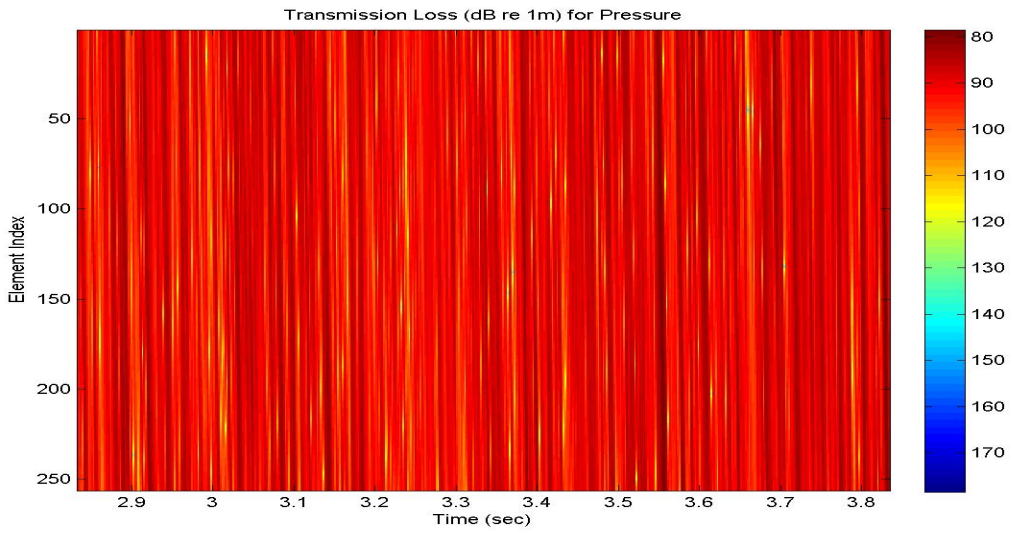

Figure 13. Time Sampled Data for Incoherent Pressure Arrival Paths

Figure 13. contains neither a spatial nor temporal processing window. Spatial and/or temporal windows can be applied in order to optimally "taper" off the amplitude of the data along the analysis window, providing better spatial and/or temporal resolution in the middle of the window and minimize discontinuities at the ends. The spatial window would be applied at each time step along the length of the array, while the temporal window would be applied at each element along the sample time.[13] In computational programs such as *Matlab*, a variety of these amplitude window functions exist. For the purposes of this thesis, we will employ a Hanning (cosine squared) spatial window to the elemental data prior to processing.

Next, a two-dimensional Fourier transform of the input data matrix is computed, such that

$$\boldsymbol{D}_p\left(K,\omega\right) = F_t F_x^{-1}\left\{\boldsymbol{D}_p\left(x,t\right)\right\} \ , \tag{4.2}$$

where F_x^{-1} represents the inverse transform along the spatial variable and F_t represents the forward transform along the time variable. This matrix then represents the transformation of the input data matrix from time-element space into K-ω space, where K represents the wavenumber component along the array,

$$K = \frac{\omega}{c}\cos\theta = \frac{2\pi f}{c}\cos\theta \ . \tag{4.3}$$

Since the frequency, and hence *K*, are discretely sampled, we can obtain the specific values of θ for each element of the matrix by

$$\cos\theta_{m,n} = \frac{K_m c}{2\pi f_n} \ . \tag{4.4}$$

The frequency values can be computed by first determining the Δf of the sampled data where

$$\Delta f = \frac{1}{T} = \frac{f_s}{N} \ . \tag{4.5}$$

The sampling frequency is f_s and the total number of time samples is *N*. Next the frequency vector is computed such that the vector is the same size as the sample time, and the frequency values themselves are then set relative to the center frequency of 1500 Hz. Since we have a total of *N* time samples, the frequency values are

$$f_j = \left(\left(j - 1 \right) - \frac{N}{2} \right) \Delta f \tag{4.6}$$

where $j = 1, ..., N$ [7].

We now wish to re-map from *K*-ω space into θ-ω space by using the above relationships. We create a vector of values, K_b, given by

$$K_b\left(i, j\right) = \frac{2\pi f_j \cos\theta_i}{c} \ , \tag{4.7}$$

where we have defined the values of θ_i over some arbitrary range, and the frequency values are computed by Equation (4.6). In the normal process of computing a pressure-only beamformer, the range of values of θ_i would range from 0 to 180 degrees relative to some fixed point along the array, usually chosen as forward end-fire. In order to better compare the output of the pressure-only beamformer to that with the vector data included, we will extend the output values of θ_i to include 360 degrees. The new range of our output angles will extend from -180 to 180 degrees, where the negative values of θ_i represent the port side of the array and the positive values represent the starboard side.

Note from the definition of the directional derivatives in Equation (2.22), this is equivalent to defining the θ_i values as ranging from 0 to 180 deg, and ϕ set to 0 deg for starboard and 180 deg for port [7].

Using the transformed data matrix in K-ω space, we can convert it into θ-ω space by first performing an interpolation of the data matrix over each frequency from K_m to K_b. The interpolation is needed in order to represent every incoming angle we desire when we do not have a sufficient number of elements to do this directly. In computational programs, such as *Matlab*, there are a number of different methods from which you can perform this interpolation. In this thesis, a cubic spline data interpolation was used because of the increased accuracy of the interpolation in comparison to other methods available [7].

Figure 14. below represents a typical θ-ω space plot converted to a θ-f space plot relative to forward end-fire (θ=0°). The mirror image on either side of end-fire results from both solutions to a plane wave response, illustrating the inherent θ ambiguity normally associated with processing pressure-only data with no other directional sensor information.

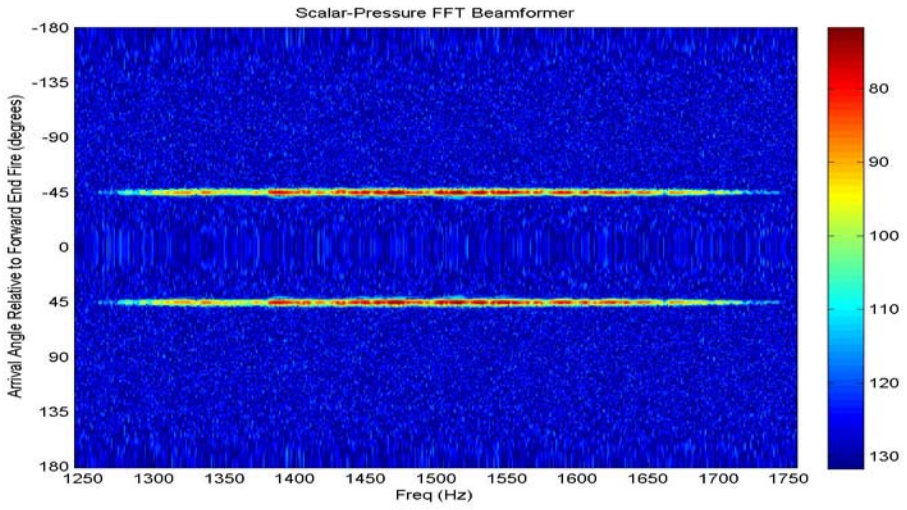

Figure 14. Natural Order Frequency vs. Angle for Pressure Data

The average spectral content can then be determined by simply summing the spectral content of each look angle and averaging the total. Figure 15 represents the average spectral content across all look angles. The 500Hz filter band (centered at 1500 Hz) for our simulated data is readily apparent in this representation.

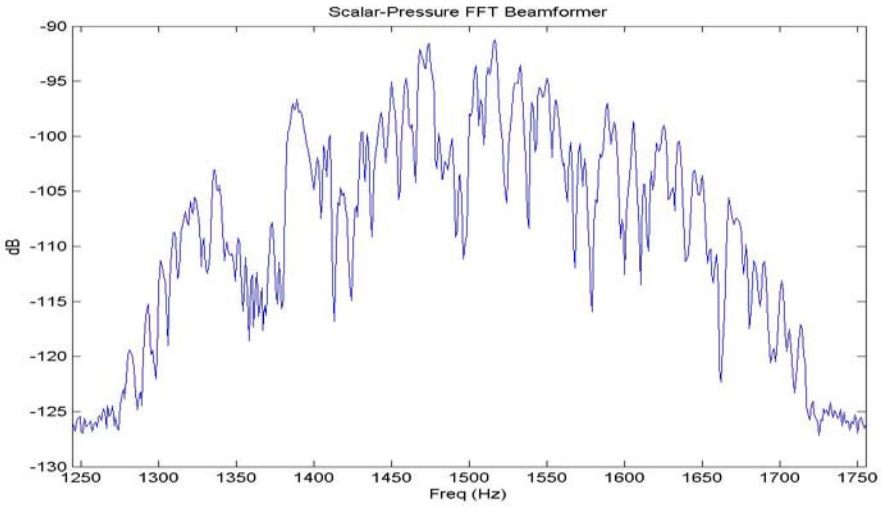

Figure 15. Average Spectral Content for Pressure Data

The data matrix can now be transformed back into the time domain by taking the inverse Fourier transform, F_{ω}^{-1}, of the data matrix across the frequency bins. This maps the data matrix from θ-ω space into θ-time space. The result is an output of arrival angle versus time. Figure 16. represents both the coherent and incoherent source pressure data in θ-time space. The data has been reoriented to show the first arrival time at the top and subsequent time moving down the y-axis. The color axis represents the output signal, in dB, referenced to the maximum received signal along the array. The nominal dynamic range of the output is 60 dB which was chosen to provide the best representation of the signal and reject very low level noise in the processing or environment [7]. This convention will be used throughout this thesis. For our test case analysis, only the incoherent data will be used in order to better represent a sustained steady signal from a distant source.

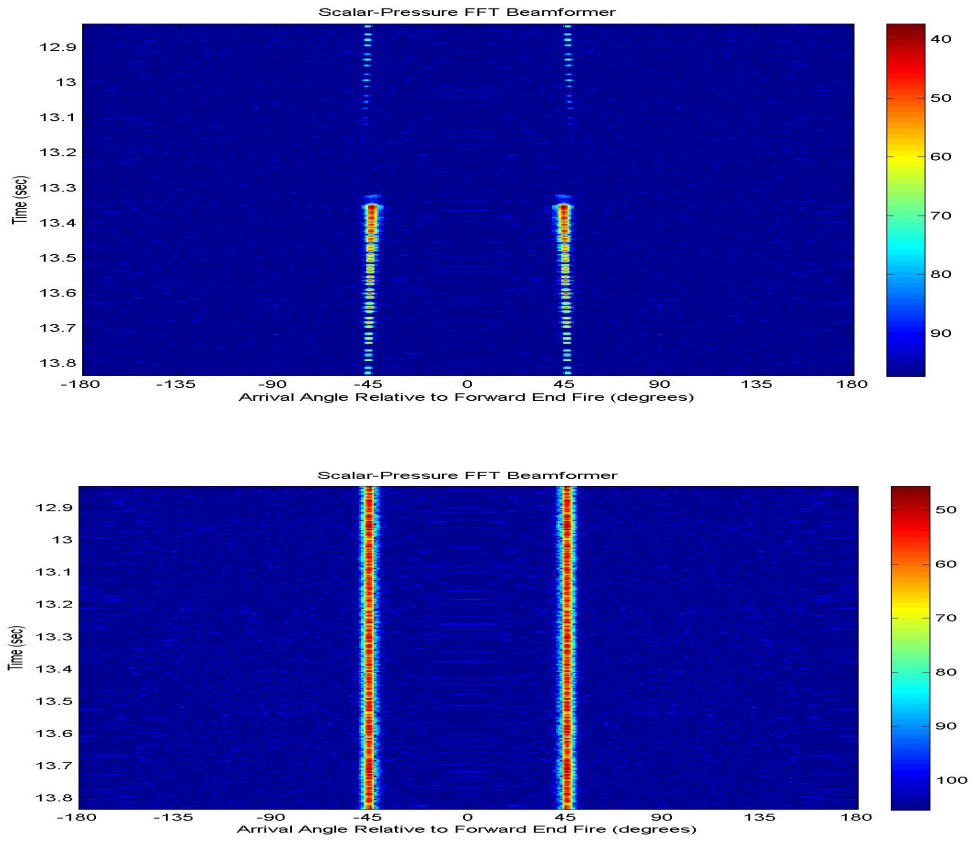

Figure 16. FFT Beamformer, Pressure-Only Coherent (Top) and Incoherent (Bottom) Data

We can then add background "noise" to each of the channels by using a Gaussian distribution random number generator referenced to the maximum received pressure magnitude at a single array element for the given source target. Thus by setting the noise magnitude at the same level as the maximum pressure magnitude reference, the signal-to-noise (SNR) ratio can be set to unity for each element of the array, providing 0dB SNR level reference, equal to 20log(SNR). This provides a method of scaling the SNR level, and thus setting a more realistic environment to our simulation. For the purposes of our analysis, we thus define our "noiseless" environment test cases at a SNR level of 40dB, whereas our "noisy" environment is set at a 0dB SNR level. Figure 17 represents the same incoherent pressure-only data in a noisy environment.

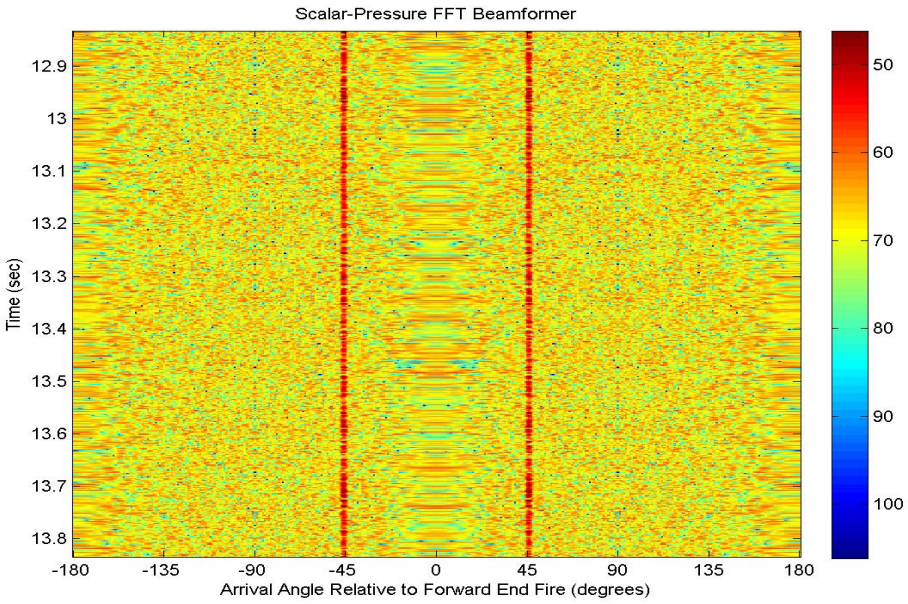

Figure 17. FFT Beamformer, Pressure-Only Incoherent Data in Noisy Environment

2. Vector Data Processing

Before processing vector data, we first must consider how to build the synthetic data matrices. Both the radial and depth components of velocity are sampled individually at the same sample frequency and with an equal number of array elements. Random phasing is applied to the velocity data in order to generate the incoherent data just as described previously with the pressure data [7]. These are illustrated below in Figure 18.

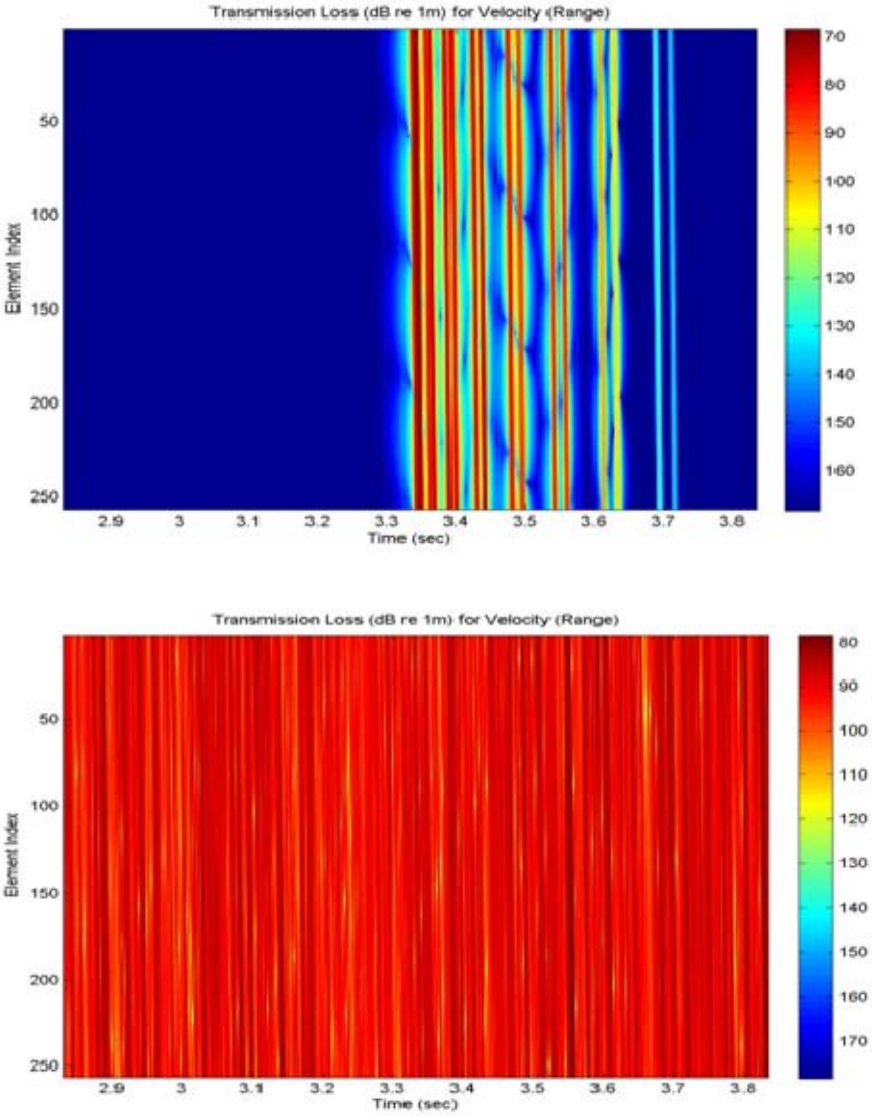

Figure 18. Time Sampled Data for Coherent (Top) and Incoherent (Bottom) Velocity Signals for Radial Vector Component

This results in four distinct, yet related, data matrices. These are represented by derived from the radial and depth components of velocity by Equation (3.27). Each of these data matrices are transformed, separately, into K-ω space and then interpolated and averaged as described above to θ-f space representation. Now the inherent advantage associated with processing the vector data is clear, as there is a distinct directional "preference" to the incoming planewave response in θ as illustrated in Figure 19 [7].

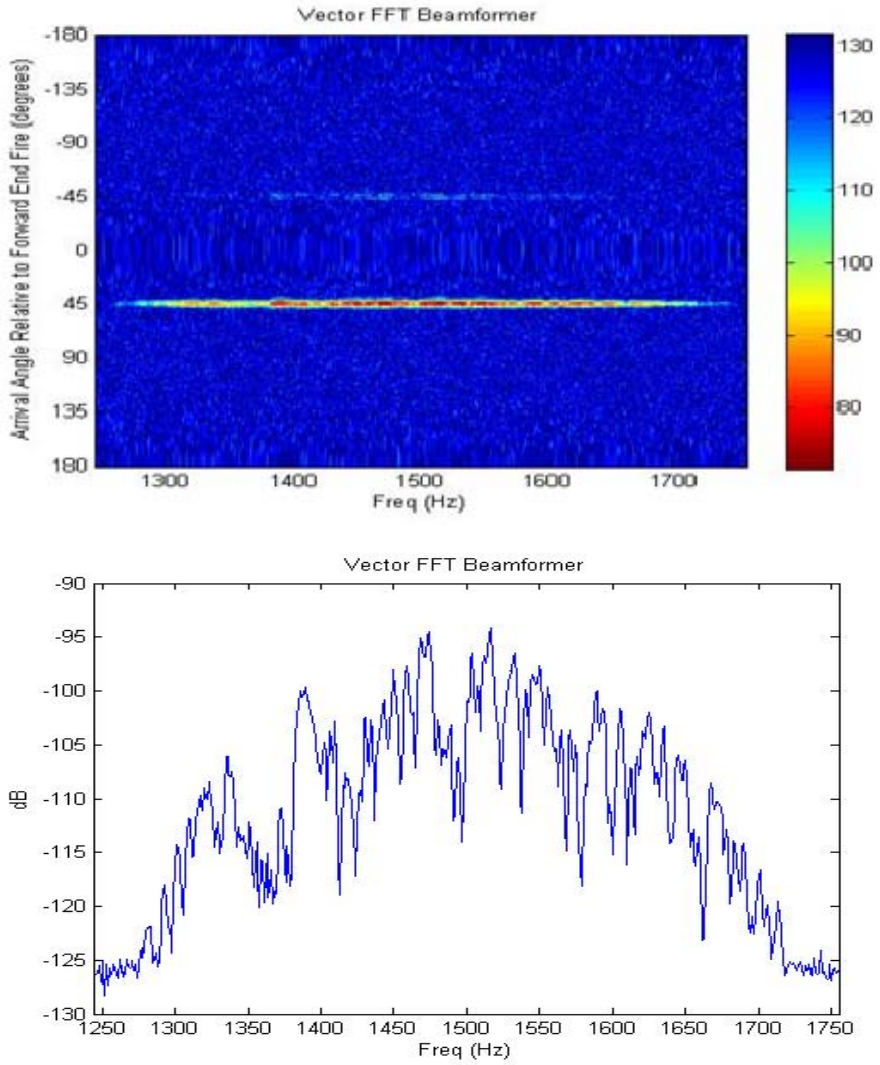

Figure 19. Natural Order Frequency vs. Angle (Top) and Average Spectral Content (Bottom) for Velocity Data

The combination of the data takes place in θ-ω space where a summation matrix of values is computed such that

$$\boldsymbol{D}_{pv} = \boldsymbol{D}_p + \boldsymbol{D}_x \rho c \cos\theta_s + \boldsymbol{D}_y \rho c \sin\theta_s \cos\phi_s + \boldsymbol{D}_z \rho c \sin\theta_s \sin\phi_s \,. \qquad (4.8)$$

This relationship both steers the velocity components of the transformed data matrices to the assumed arrival angle of the incoming plane wave and rescales the velocity values by the factor ρc for normalization with the pressure data. We use the same range of θ_i given in the pressure-only processing, -180 to 180 degrees, and represent the angle

relative to forward end-fire in the xy-plane. The elevation angle, ϕ, represents the angle relative to the vertical depth axis, referenced to starboard. In this case, we only allow values of 0 or 180 deg. Thus, we neglect the vertical velocity component in Equation (3.35). Finally, the inverse Fourier transform, F_{ω}^{-1}, of the resulting combined data matrix, $\boldsymbol{D}_{pv}$, is taken, which produces the plot in Figure 19. Again, however, only the incoherent data will be used in our further analysis.

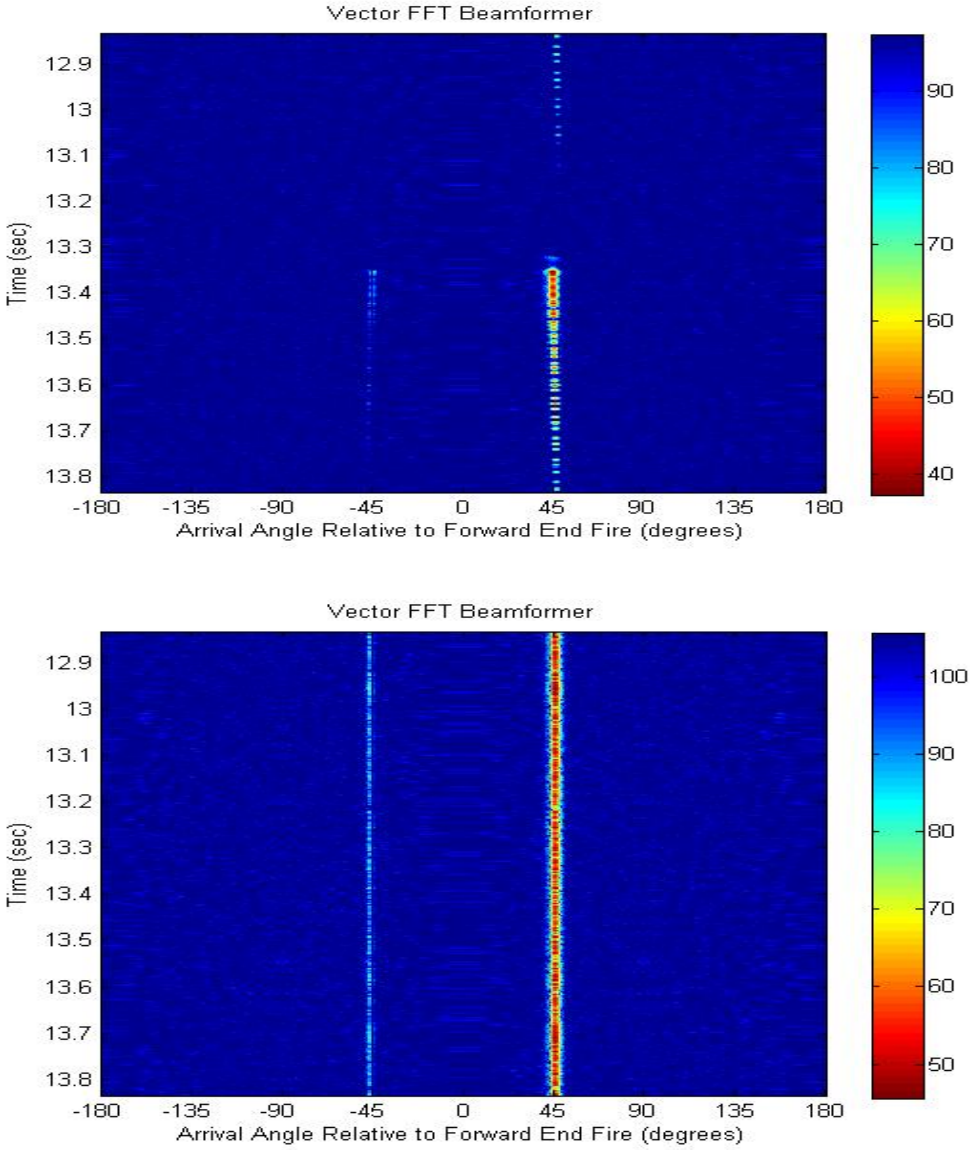

Figure 20. Time Sampled Data for Coherent (Top) and Incoherent (Bottom) Arrival Paths

As before, the vector data can be set to exhibit random noise relative to the maximum received pressure level at a single array element for the given source target, thus allowing SNR level to be controlled for the velocity channels as well for both a "noiseless" and "noisy" environment illustrated in Figure 21.

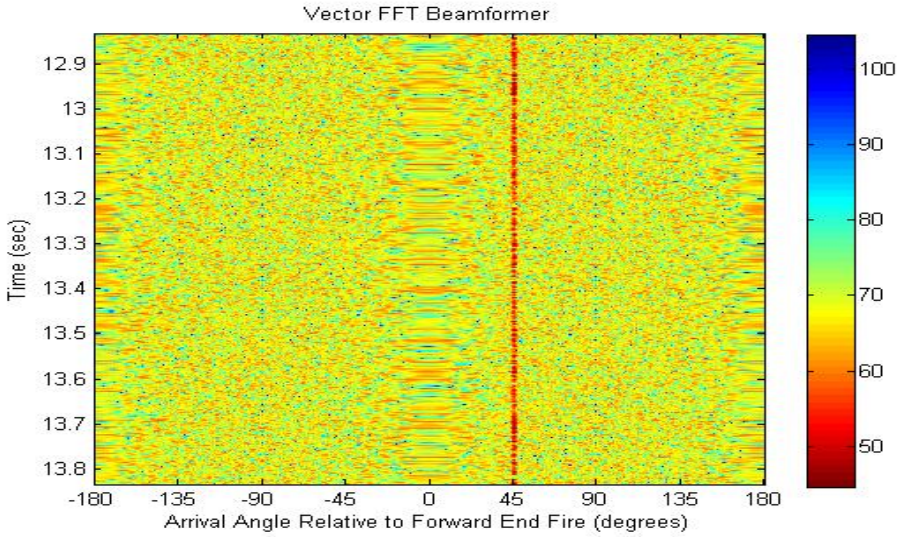

Figure 21. FFT Beamformer, Vector Incoherent Data in Noisy Environment

The data can then be summed across time for each of the 360 look angles, and divided by the number of time samples (N = 512) such that the data is "time-averaged" over the analysis window across each look angle. Although a simple processing technique, it can nonetheless prove to be a powerful tool in signal recognition given a sufficient time span for both high and low SNR sources. In Figure 22 below, the correct target aspect (dashed red line) is clearly distinguishable in both the noiseless and noisy environment with vector processing, and made more recognizable by time averaging.

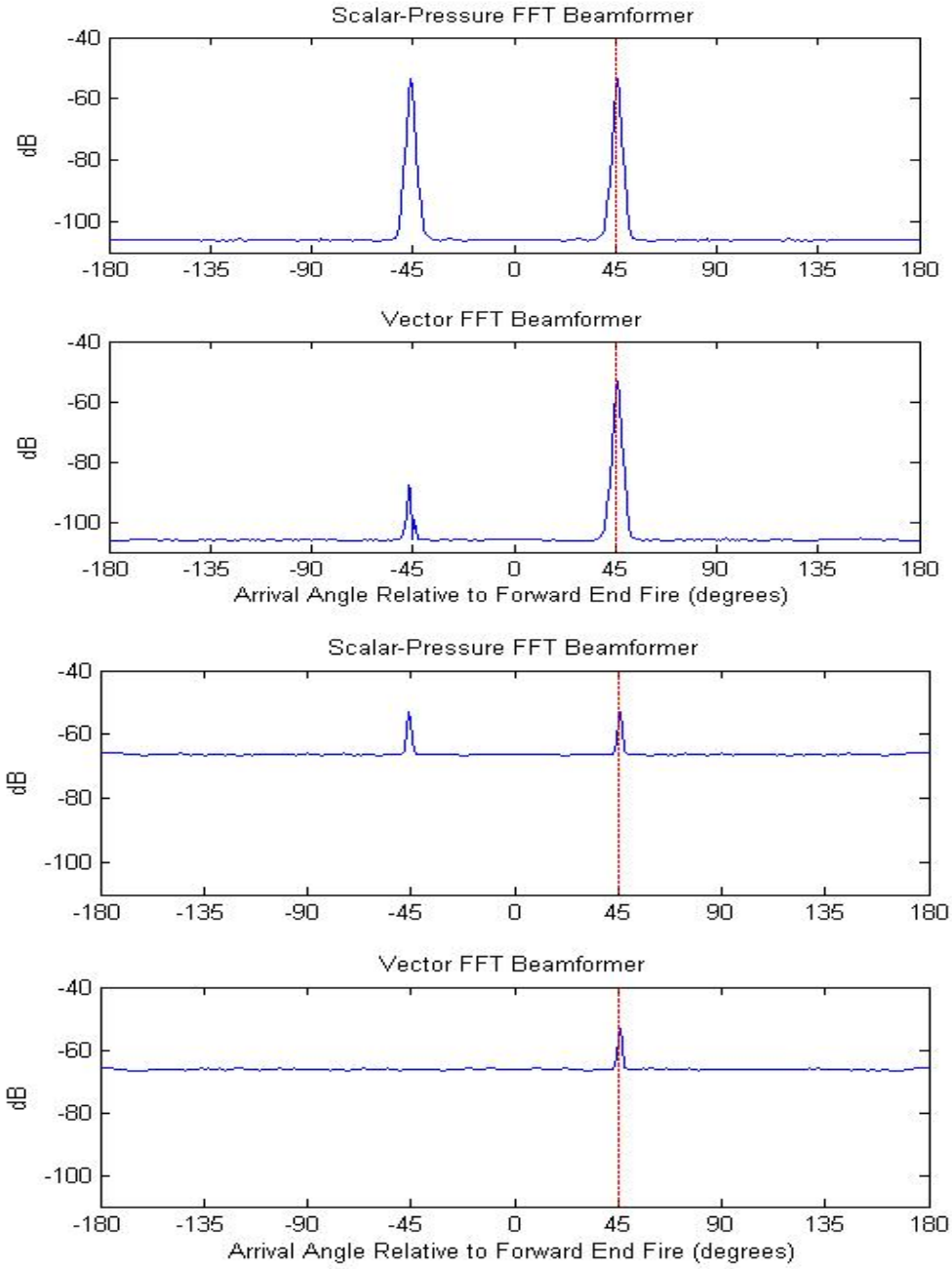

Figure 22. Time Averaged Pressure and Vector Signal Data for Both Noiseless (Top Set) and Noisy Environment (Bottom Set)

By processing the pressure and velocity data separately and scaling appropriately, we create the flexibility necessary to more efficiently “build” the beamformed processors described in Chapter II, as the inherent differences between each unique processor are then simply a function of applied weighting and combinations of separately processed weightings. Similarly, individual weightings can be scalar amplified to enhance or degrade the properties of those beams as necessitated by the background noise level, as we shall demonstrate.

Both the color and time-averaged dB plots will be used throughout this thesis as a side by side comparison tool of both the cardioid and optimal weighting to the scalar-pressure processor, as well as the various other processors to the baseline cardioid for both single element and linear array analysis. The metrics to be measured will then be look directivity gain (relative to the pressure-only case) and noise level change (from the high SNR to low SNR environment) in the look direction for the single element case. This will provide insight into our array analysis, where we will compare SNR gain (relative to the noise floor) and ambiguity rejection (difference in look direction intensity and conjugate angle intensity) for the array case. These metrics will be tested in both high and low SNR environments where applicable.

THIS PAGE INTENTIONALLY LEFT BLANK

V. SIMULATION RESULTS

A. DATA SOURCES

The data generated using the MMPE model consisted of six distinct sources at different ranges, depths and aspect angles, as given in Table 1.

Source	Range (km)	Depth (m)	Bearing
1	20	45	45
2	10	5	80
3	18	7	100
4	15	30	-50
5	12	35	-105
6	0.2	40	0

Table 1. Sound Sources

The geometry of the source locations, as seen from above, is shown in Figure 23, where the bearing represents the angles bearing from forward endfire. These were chosen to allow for different combinations of sources that could prove difficult or challenging for pressure only beamforming techniques to determine where they are located, such as sources on nearly ambiguous angles but opposite sides of the array. Source 6 is used to simulate a tow-ship for the array, located 200 meters directly in front of the array at the same depth of 40 meters, thus representing the only "near-field" source of Equation (3.27). This combination of signal data easily allows for variations in source levels between the different targets of interest when setting a common source level of 0 dB [7]. The exception will be Source 2, which is set 20dB higher than the other sources in order to represent a loud interfering source.

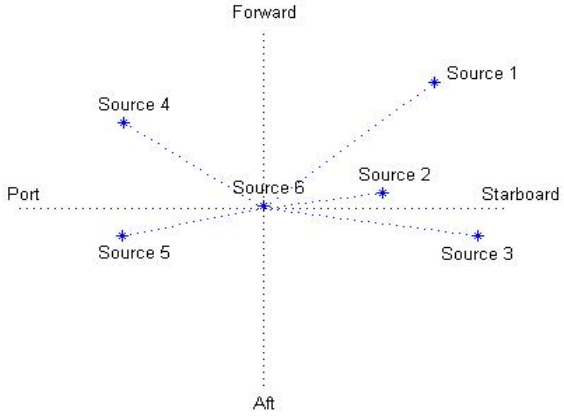

Figure 23. Source Geometry

Our shallow water environment is represented by a 1500m/s isospeed sound speed profile (SSP) coupled to a singular, zero-elevation bottom type for simplicity, with the properties given in Table 2 [7].

Bottom Depth (m)	150
Sound Speed (m/s)	1600
Bottom Density (g/cm^3)	1.2
Attenuation, α (dB/km/Hz)	0.1

Table 2. Bottom Data

B. SINGLE ELEMENT ANALYSIS

Using the FFT beamforming algorithms discussed, we can thus combine the pressure and velocity component signal contributions for a single element response to our two test sources 1 & 3 (45°, 100°). When employing the standard FFT cardioid beamformer weighting of Equation (2.25), for a single element response, the added directionality obtained is apparent, as well as the theoretical gain over the conventional scalar pressure counterpart in Figure 24. As expected, for the single element cardioid, beam response is independent of look direction, and the steer angle is in the look direction ($\theta_s = \theta$).

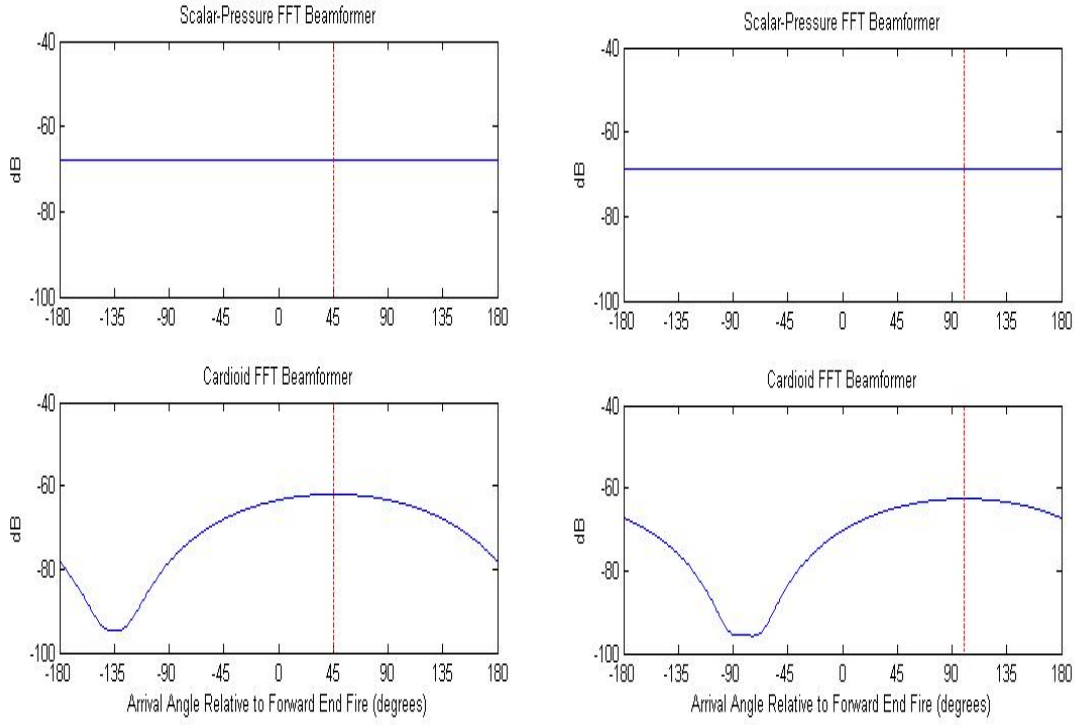

Figure 24. Single Element Cardioid and Scalar Pressure Comparison for Sources 1 & 3 (45°,100°)

When we add noise to the single element and take the SNR level to 0dB, the directionality begins to degrade, as well as the look direction gain, since the channel noise level is set to the pressure and vector input signal contribution, as illustrated in Figure 25.

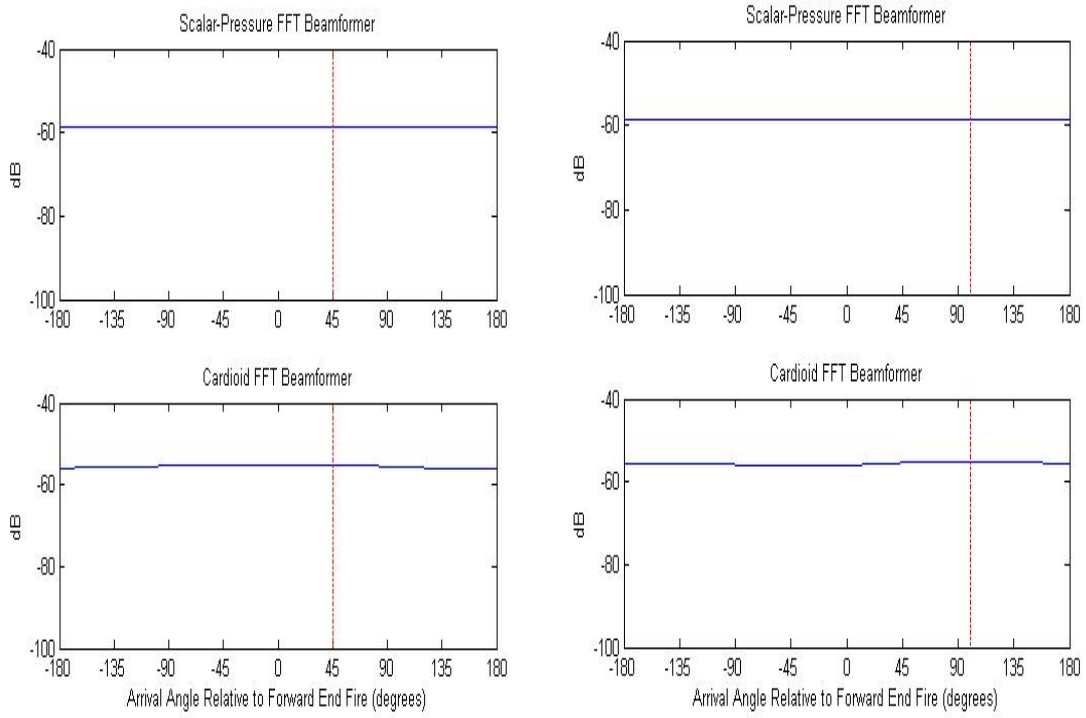

Figure 25. Single Element Cardioid and Scalar Pressure Comparison for Sources 1 & 3 (45°,100°) in Noisy Environment

When we apply optimal weighting of Equation (2.27), the FFT beamformer now increases the look direction signal gain and decreases the main lobe width from the cardioid response as expected, but at the expense of creating a significant backlobe.

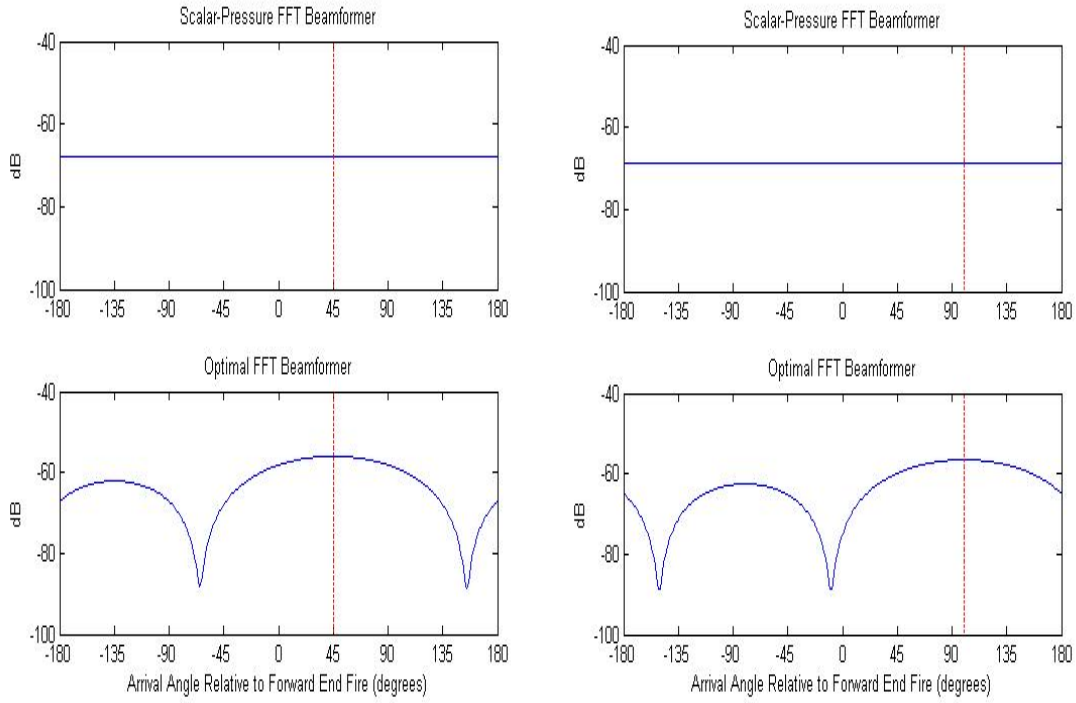

Figure 26. Single Element Optimal and Scalar Pressure Comparison for Sources 1 & 3 (45°,100°)

However, when the noise in the channel is increased, the increased weighting factor becomes detrimental to performance, as directionality becomes increasingly ambiguous and gain in the look direction decreases dramatically.

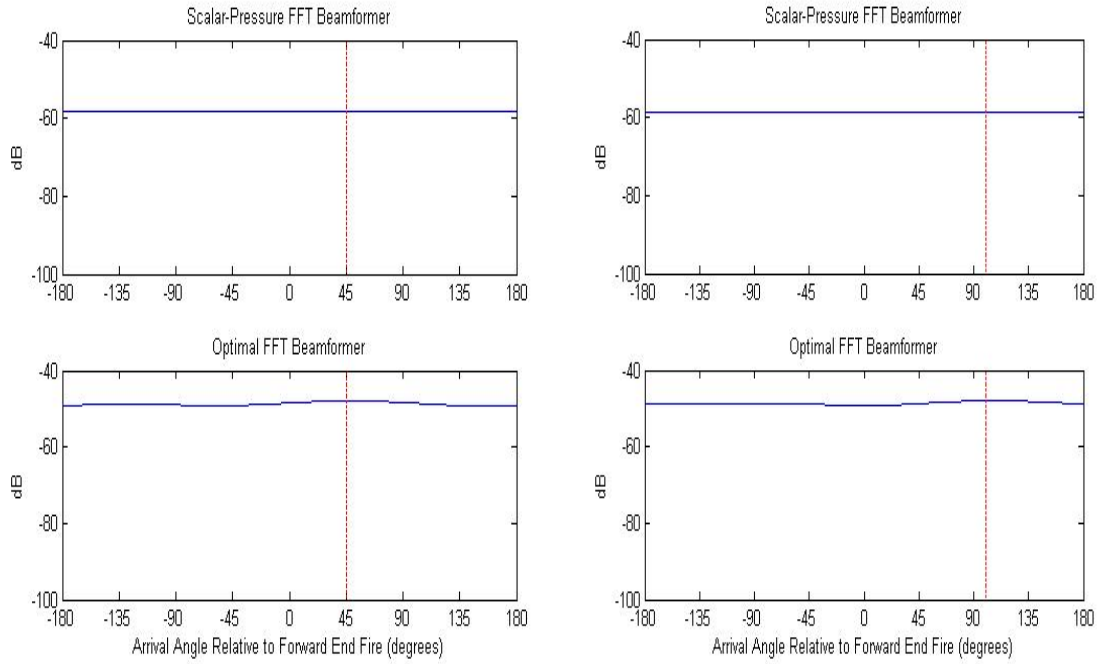

Figure 27. Single Element Optimal and Scalar Pressure Comparison for Sources 1 & 3 (45°,100°) in noisy environment

Applying the dynamic null-steering weighting of Equation (2.30), and comparing to the similarly weighted cardioid displays the inherent problem associated with single element null-steering, as the "skew" from the peak response for off-broadside look angles is readily apparent, thus rendering true target aspect problematic in the single element case. However, the null is now steered to the ambiguous angle for both test sources 1 and 3 (45°,100°), which will be of higher application in linear array analysis.

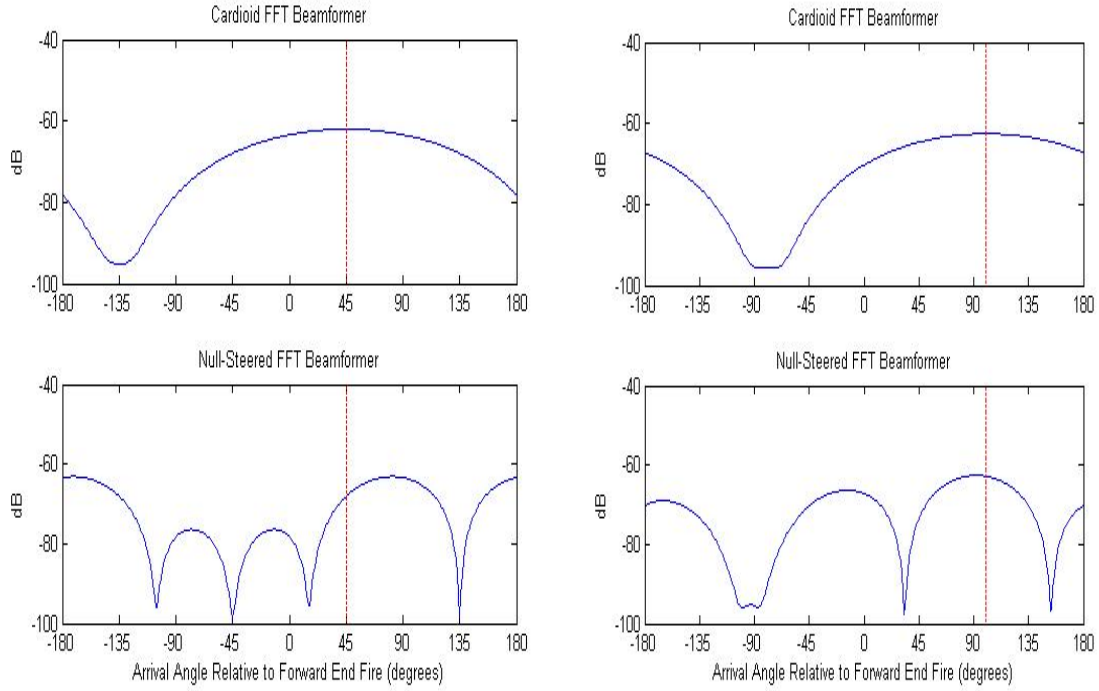

Figure 28. Single Element Dynamic Null-Steered and Cardioid Comparison for Sources 1 & 3 (45°,100°)

Increased ambiguity ensues when additional noise is added, as the dynamic null itself gets "washed" out when the SNR level is taken to 0dB. This curious effect is due to the dynamic null-steered pressure weighting dominating over both signal and noise, evident in the time averaged plot in a noisy environment.

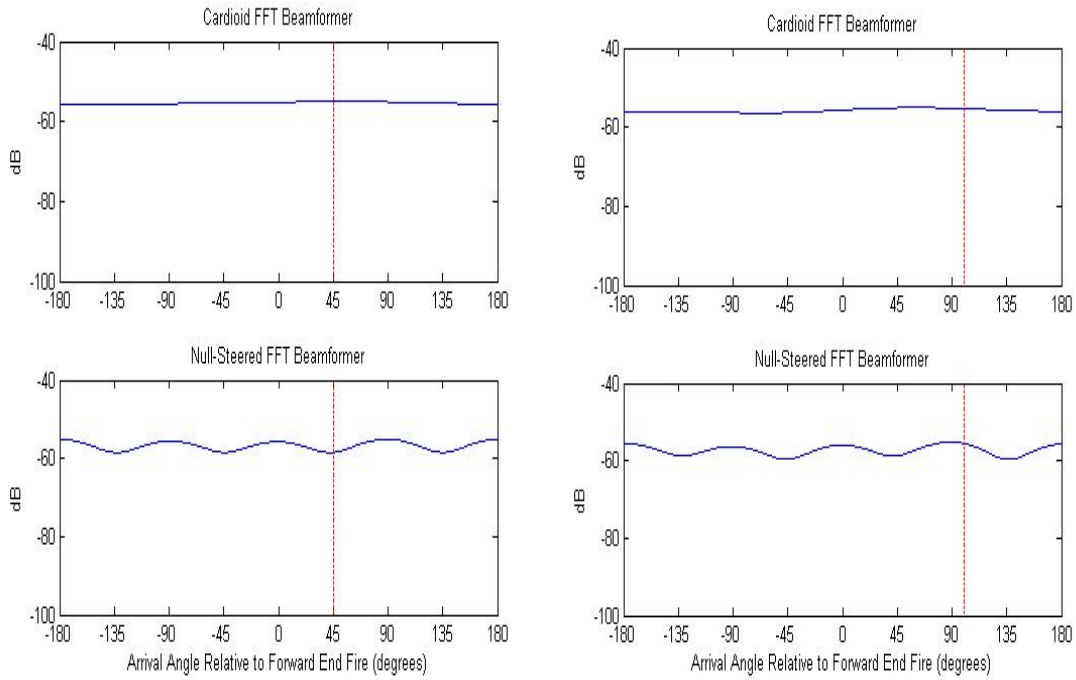

Figure 29. Single Element Dynamic Null-Steered and Cardioid Comparison for Sources 1 & 3 (45°,100°) in Noisy Environment

A summary of single element array performance is presented in Tables 3 and 4, where we are comparing directivity gain (relative to the pressure-only sensor) and noise increase in the look direction (relative to the low SNR case. Both the cardioid and optimal weighting appear to conform to earlier predictions of 6dB and 12dB look direction signal gain respectively, and it is thus apparent that in high SNR environments, the optimal linear weighting $(w_{xn} = w_{yn} = w_{zn} = 3; w_{pn} = 1)$ can have distinct benefits over the uniform weighting $(w_{xn} = w_{yn} = w_{zn} = w_{pn} = 1)$ in both look direction gain and

decreased main lobe width. However, optimal weighting is outperformed by the uniform cardioid weighting in lower SNR environments, where channel noise dominates the increased directional weighting. This will be a more significant factor in the array analysis. The other weighting schemes provide little to no benefit for the single element case.

SINGLE ELEMENT	SNR level = 40dB	
	Source 1 (45°)	Source 3 (100°)
	Δ Direct (dB)	Δ Direct (dB)
Scalar Pressure	0	0
Cardioid	5.98	6.04
Optimal	**11.94**	**12.05**
Dynamic Null-Steered	-.10	5.80

Table 3. Single Element Comparison Summary for Noiseless Environment

SINGLE ELEMENT	SNR level = 0dB	
	Source 1 (45°)	Source 3 (100°)
	Δ Noise (dB)	Δ Noise (dB)
Scalar Pressure	9.13	9.68
Cardioid	**6.75**	**7.19**
Optimal	7.82	8.44
Dynamic Null-Steered	9.79	7.34

Table 4. Single Element Comparison Summary for Noisy Environment

C. LINEAR ARRAY ANALYSIS

When examining the results of the full vector sensor array processing, the standard cardioid beamformer clearly proves its superiority over conventional pressure-only processing. A distinct gain in the look direction is observed in the high SNR case, as well as a clear rejection of the conjugate angle, especially apparent for source 2 (100°), is illustrated for the cardioid array in Figure 30. It can be noted that for source 1 (45°), however, this ambiguity rejection is less apparent, as expected of contacts further away from broadside due to the relative null placement of the individual cardioid weightings.

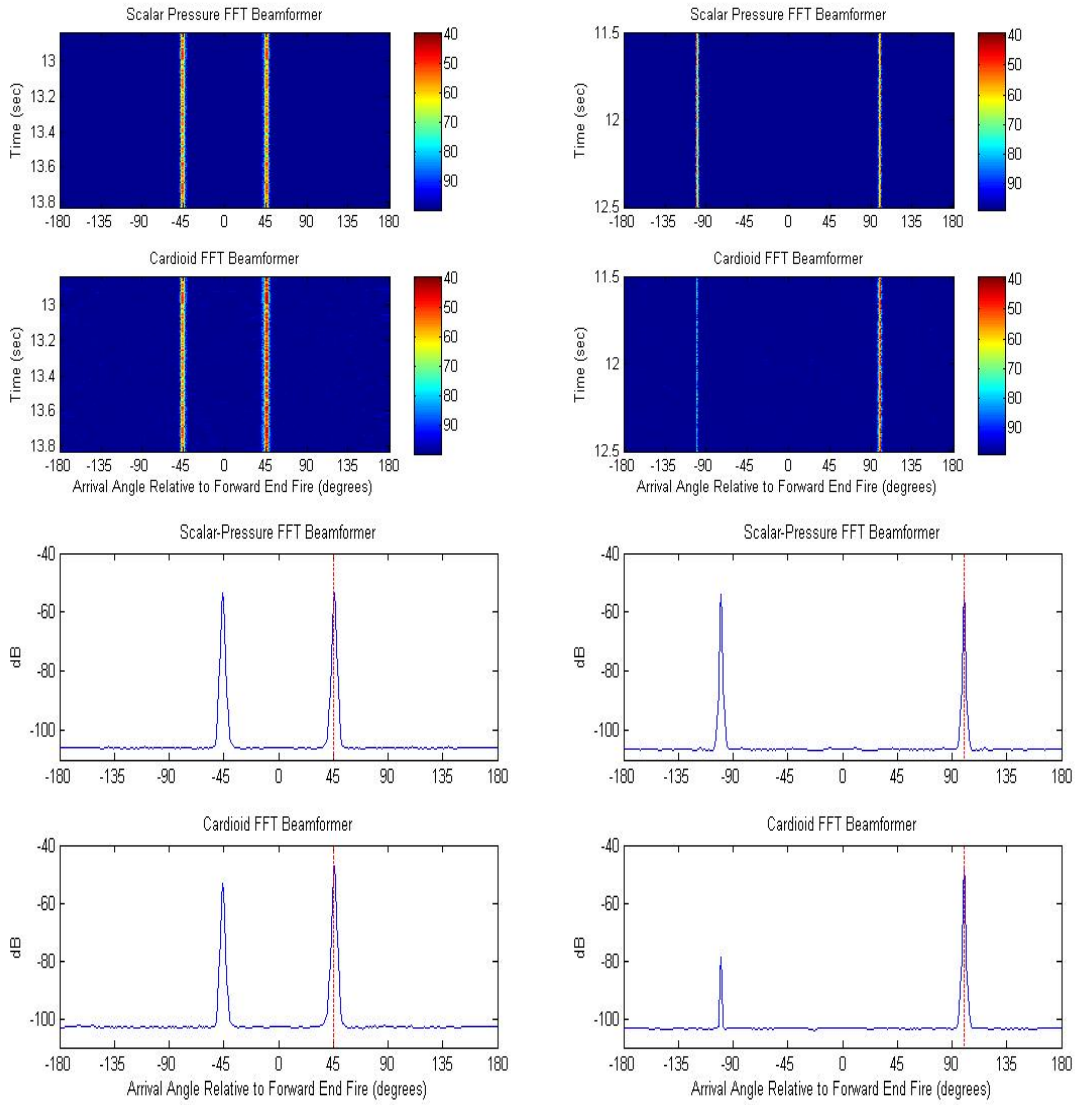

Figure 30. Cardioid and Scalar Pressure Array Comparison for Sources 1 & 3 (45°,100°)

When we increase the environmental noise, the standard cardioid processor holds relatively well in terms of signal gain in the look direction and relative ambiguity rejection, as observed in the Figure 31 below. It is interesting to note that the ambiguity is essentially "washed" out by the noise floor in low SNR environments for Source 3.

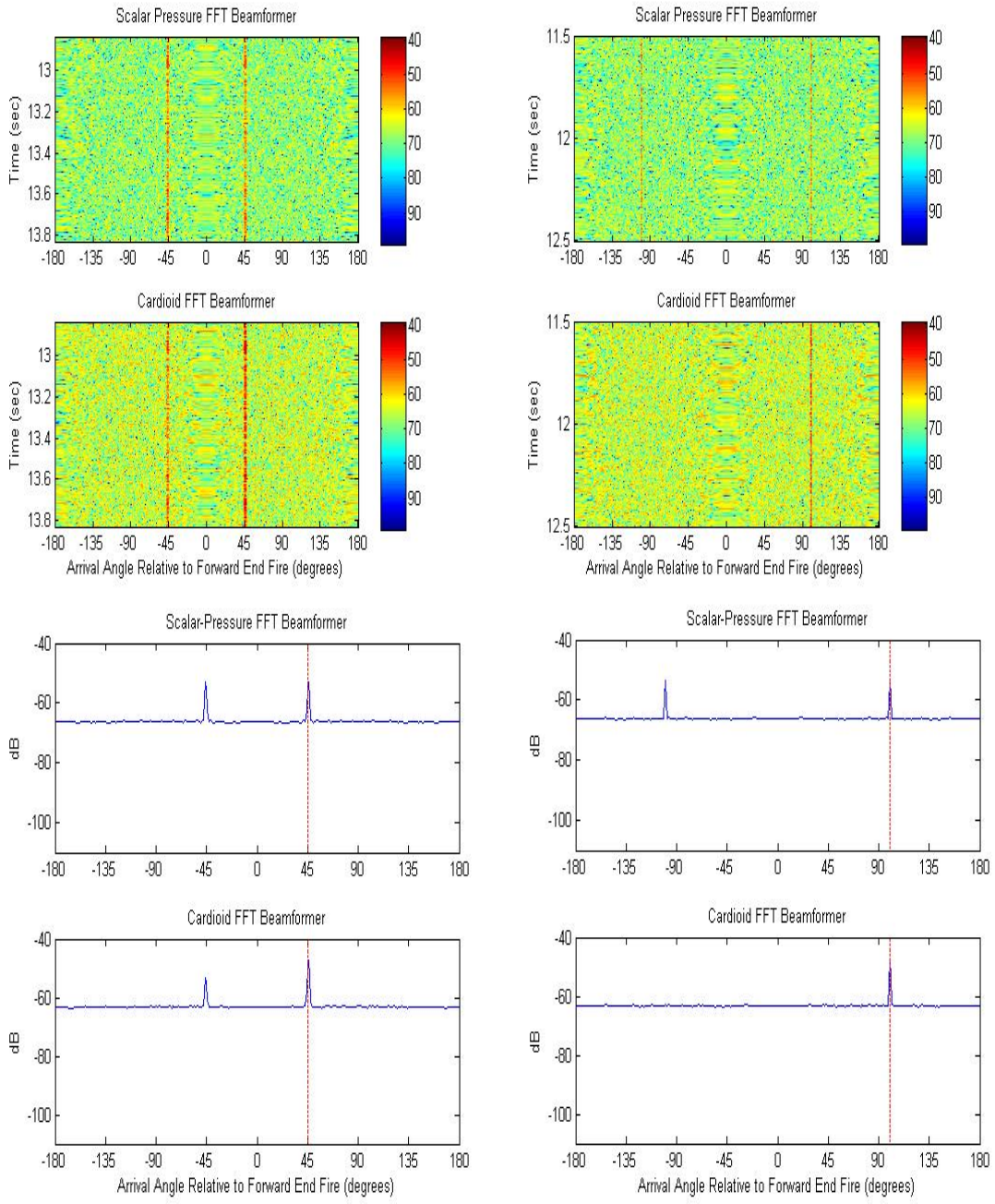

Figure 31. Cardioid and Scalar Pressure Array Comparison for Sources 1 & 3 (45°,100°) in Noisy Environment

Optimal weighting in low noise environments increases signal gain in the look direction, as expected in Figure 32, with a tendency to favor targets further away from broadside in terms of ambiguity rejection due to the relative null placement of the individual optimal weightings.

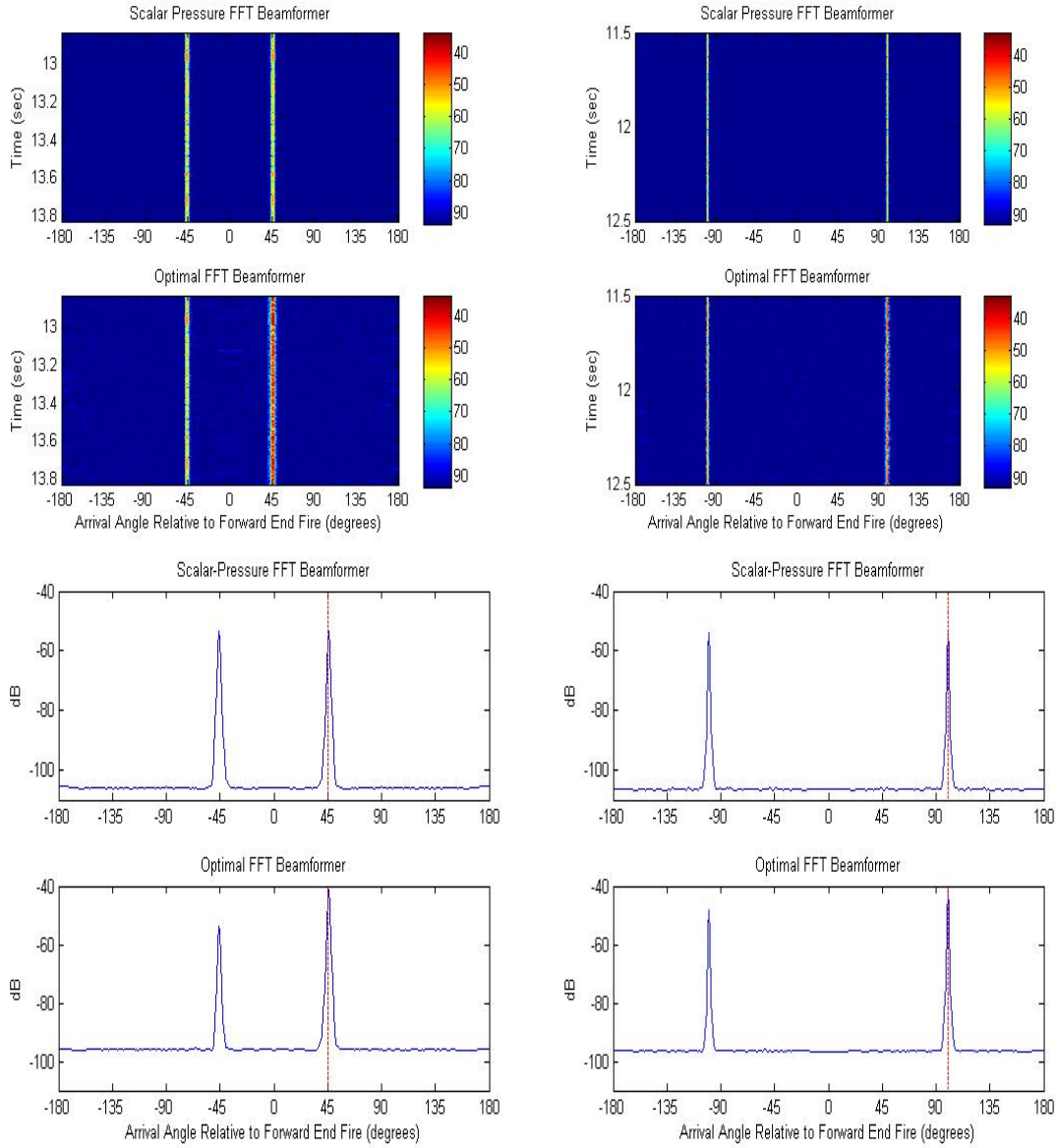

Figure 32. Optimal and Scalar Pressure Array Comparison for Sources 1 & 3 (45°,100°)

With increased channel noise, the optimal weighting processor shows similar ambiguity "washout" for Source 1 but drastic signal recognition loss for Source 3 in

Figure 33. Overall, the optimal weighted array suffers drastic SNR loss in the look direction relative to the noise floor due to increased channel noise of the weighted velocity elements.

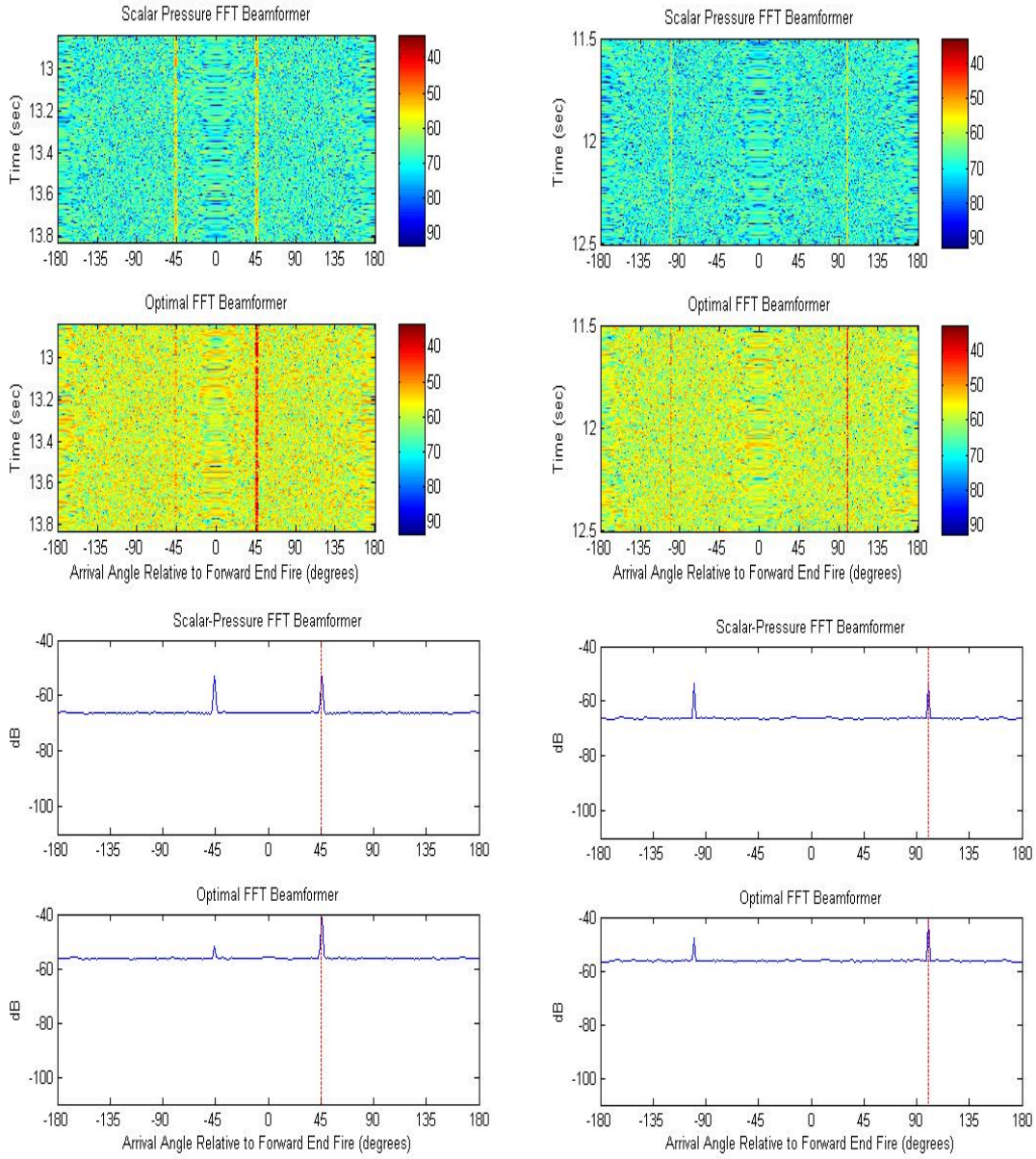

Figure 33. Optimal and Scalar Pressure Array Comparison for Sources 1 & 3 (45°,100°) in Noisy Environment

The shortcomings of common vector array steering along different look angles for fixed null weighting is apparent in both the cardioid and optimal case. The benefits of

dynamic null-steered weighting, then, are readily apparent in Figure 34, displaying remarkable ambiguity rejection at high SNR regardless of look angle. It is apparent that common vector steering of a multi-element array of dynamic null-steered elements now matches peak response in the look direction, though the array suffers decreases in look direction signal gain when compared to standard cardioid processing for off-broadside look angles due to "skew" effects of the individual elements.

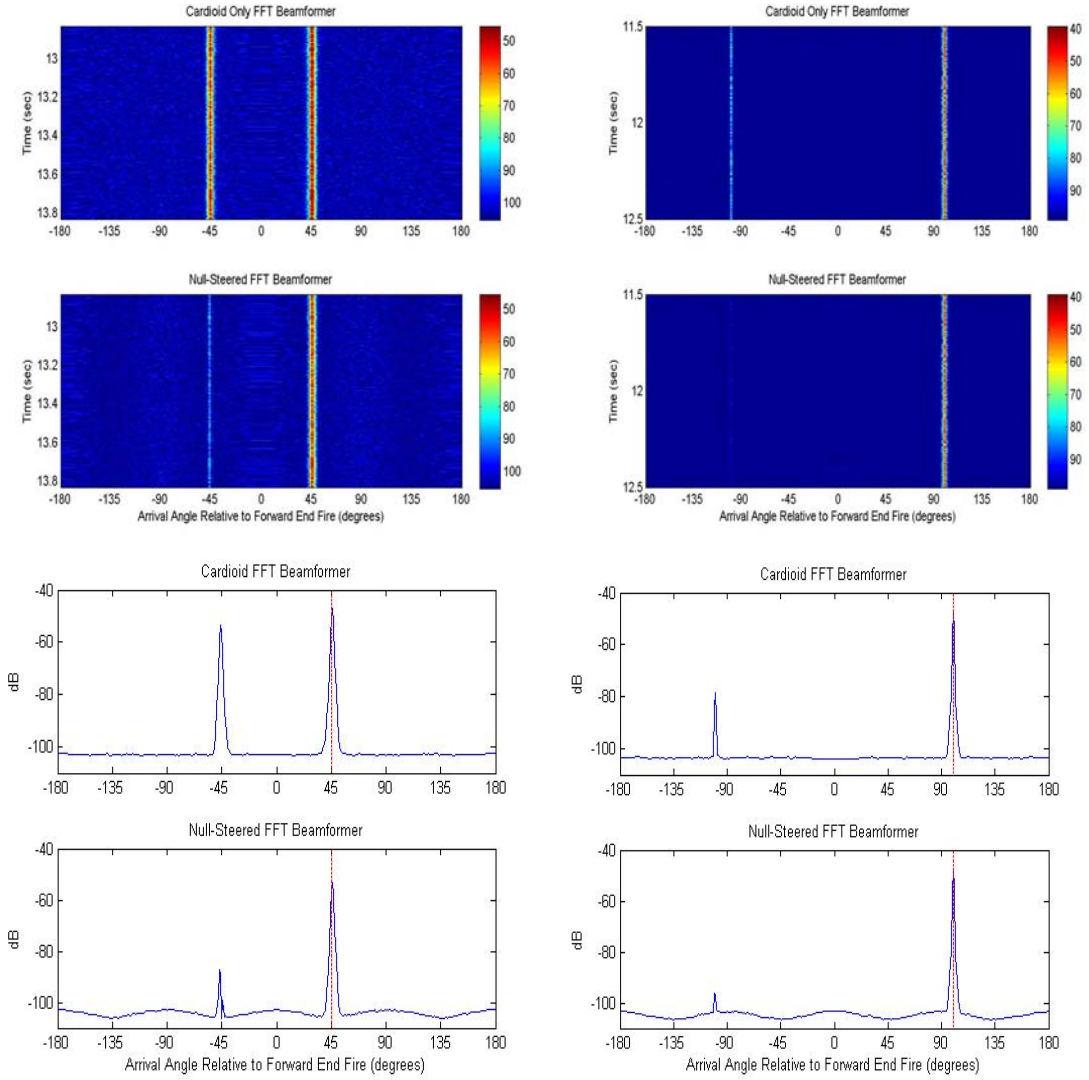

Figure 34. Dynamic Null-Steered and Cardioid Array Comparison for Sources 1 & 3 (45°,100°)

In noisier environments, the dynamic null-steered processor begins to suffer from large fluctuations in the noise floor due to the dynamic null pressure weighting. Although

the increased noise floor washes out ambiguity for both Sources 1 and 3, the overall signal gain is still less than the cardioid processor for both sources in Figure 35.

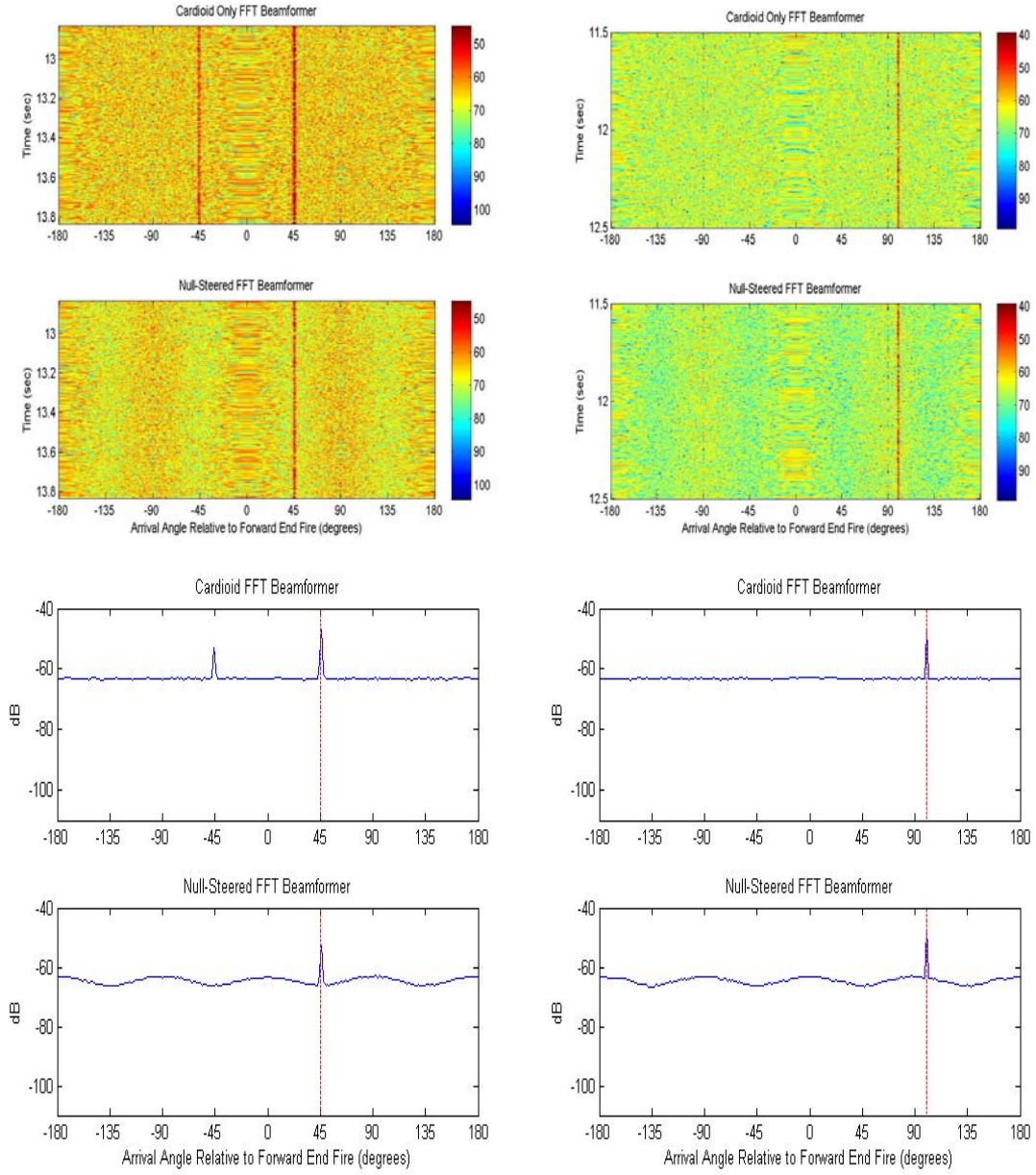

Figure 35. Dynamic Null-Steered and Cardioid Array Comparison for Sources 1 & 3 (45°,100°) in Noisy Environment

D. NONLINEAR ARRAY ANALYSIS

One approach to combine the positive benefits of the different beamformers previously described is to take the product of the outputs of two separately processed beams to form a nonlinear, hybrid processor.

The "cardynull" essentially combines the benefits of the standard uniformly weighted cardioid ($w_{xn} = w_{yn} = w_{zn} = w_{pn} = 1$) with the unique properties of dynamic null-steering ($w_{xn} = w_{yn} = w_{zn} = 1; w_{pn} = -\cos(2\theta_s)$) in order to provide better directivity and ambiguity rejection at all look angles.

Another train of thought seeks to achieve higher directivity by utilizing a combination of beamshapes. Thus, the "hippioid"[6] involves the beamform combination of the standard uniformly weighted cardioid ($w_{xn} = w_{yn} = w_{zn} = w_{pn} = 1$) and a vector-only dipole ($w_{xn} = w_{yn} = w_{zn} = 1; w_{pn} = 0$).

Both the cardynull and hippioid have similar advantages over the standard cardioid in both low and high noise environments for off-broadside sources in terms of look angle directivity gain and ambiguity rejection. However, only the cardynull can compete with the cardioid in both low and high noise environments for sources near broadside, as can be observed in Figures 36-39, as the hippioid suffers poor ambiguity rejection at these angles, as expected, due to the dipole beamformer component.

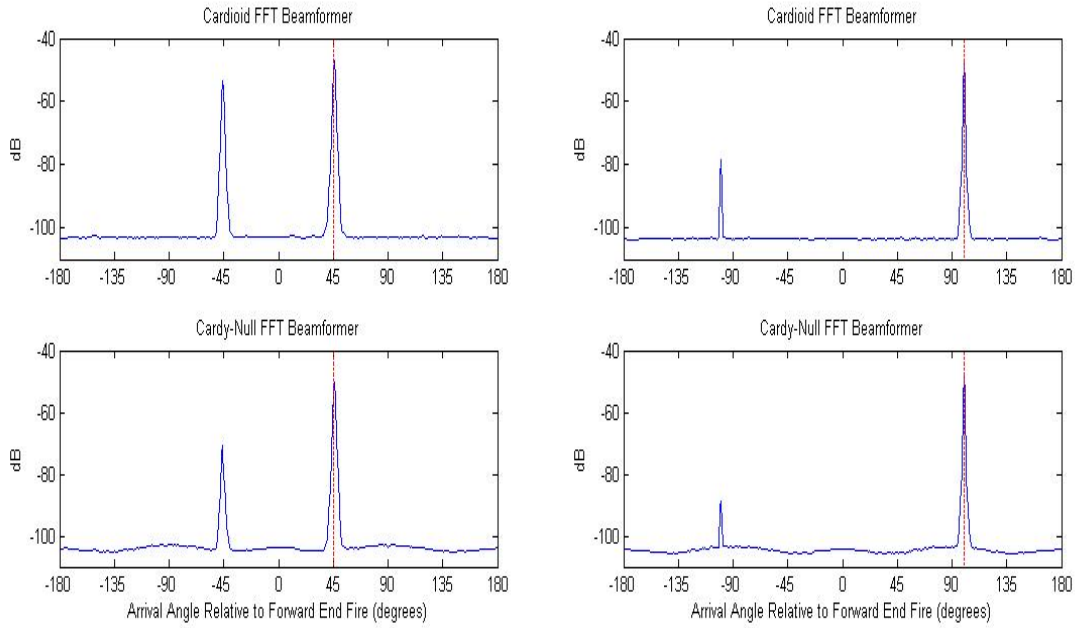

Figure 36. Cardynull and Cardioid Array Comparison for Sources 1 & 3 (45°,100°)

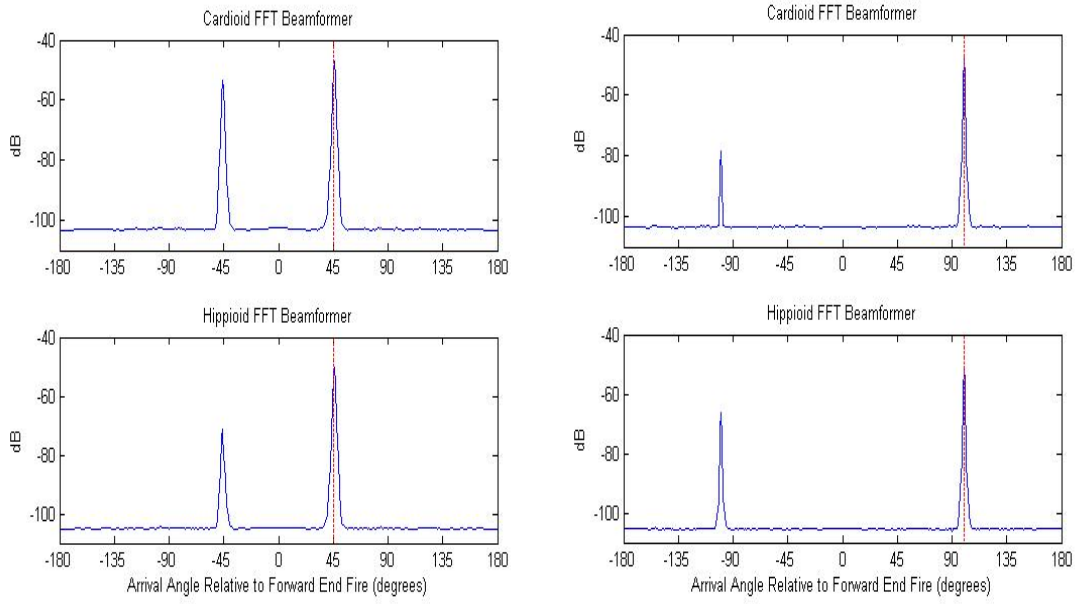

Figure 37. Hippioid and Cardioid Array Comparison for Sources 1 & 3 (45°,100°)

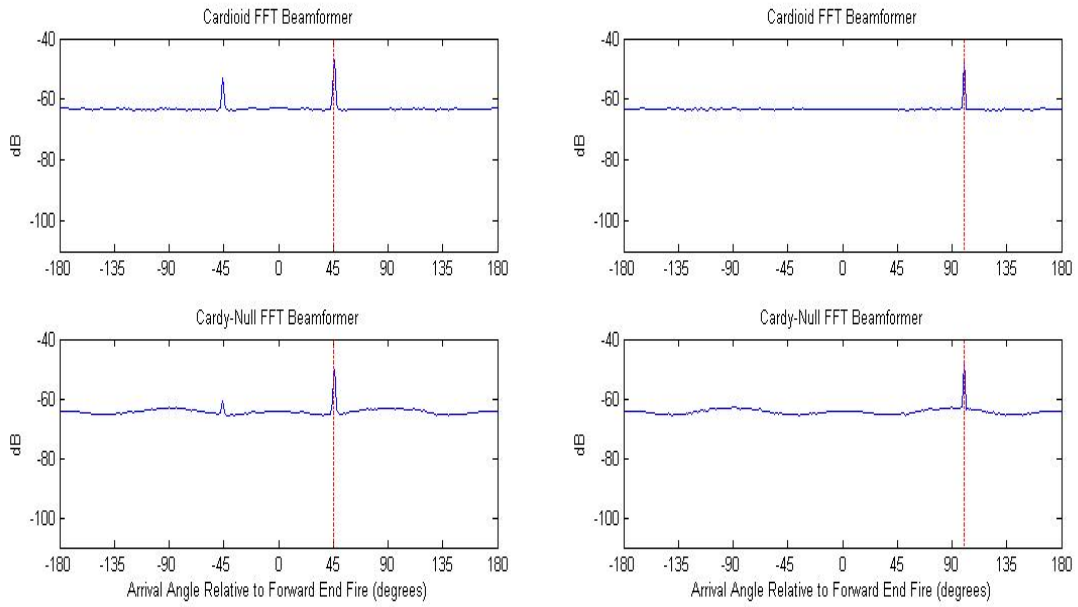

Figure 38. Cardynull and Cardioid Array Comparison for Sources 1 & 3 (45°,100°) in Noisy Environment

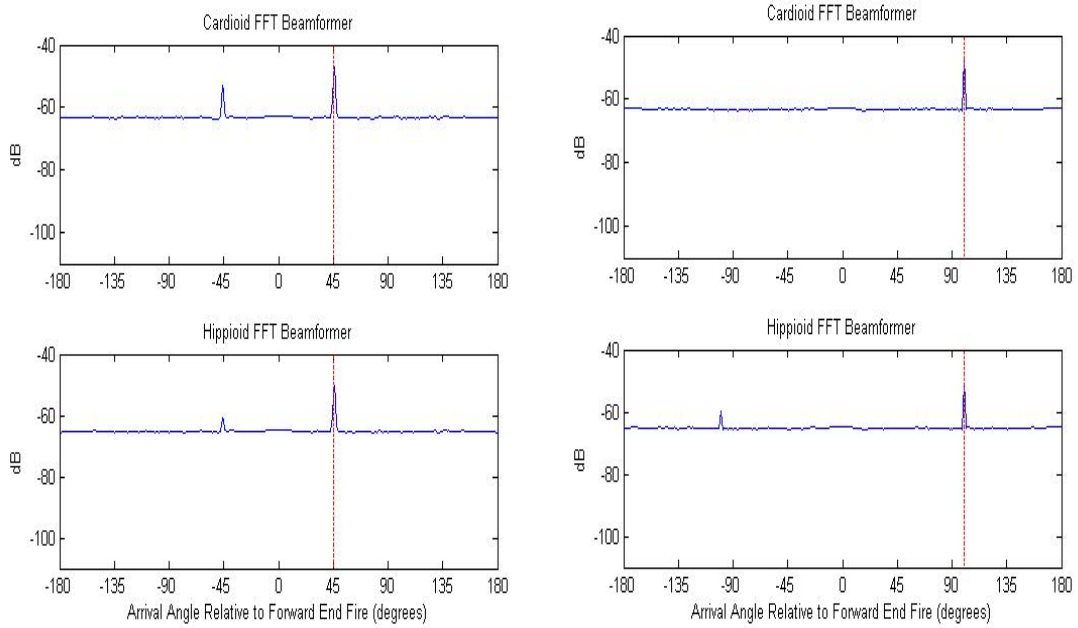

Figure 39. Hippioid and Cardioid Array Comparison for Sources 1 & 3 (45°,100°) in Noisy Environment

The overall performance comparisons, in terms of look direction SNR gain (relative to baseline noise floor) and ambiguity rejection (relative to conjugate angle), are summarized in Tables 5 and 6. For noiseless environments, optimal weighting provides the highest SNR gain in the look direction whereas dynamic null-steering provides the best ambiguity rejection. However, for noisy environments, standard cardioid weighting provides the best SNR look direction gain, and dynamic null-steering still provides the best ambiguity rejection (though not necessarily for all look angles). Cardynull processing appears to be a compromise between the two in most cases. It can be noted that the directivity gain in the look direction of 6dB and 12dB respectively holds for both the cardioid and optimal weighting in high SNR environments, but only the cardioid retains the same directivity gain in the low SNR case.

ARRAY	SNR level = 40dB			
	Source 1 (45°)		Source 3 (100°)	
	Δ SNR (dB)	Δ Reject (dB)	Δ SNR (dB)	Δ Reject (dB)
Scalar Pressure	44.7	0	46.27	0
Cardioid	50.7	5.95	52.3	30.89
Optimal	**56.69**	11.94	**58.33**	6.82
Dynamic Null-Steered	44.75	**34.75**	52.03	**49.01**
Cardynull	47.66	29.12	52.16	40.78
Hippioid	47.66	29.09	49.29	15.73

Table 5. Array Comparison Summary for Noiseless Environment

ARRAY	SNR level = 0dB			
	Source 1 (45°)		Source 3 (100°)	
	Δ SNR (dB)	Δ Reject (dB)	Δ SNR (dB)	Δ Reject (dB)
Scalar Pressure	10.2	0	11.1	0
Cardioid	**15.84**	5.6	**17.36**	15.64
Optimal	11.91	9.54	13.49	6.29
Dynamic Null-Steered	9.93	**10.98**	17.13	15.38
Cardynull	12.85	9.37	17.27	**15.82**
Hippioid	12.94	9.42	14.4	8.98

Table 6. Array Comparison Summary for Noisy Environment

E. MULTIPLE SOURCES

The inherent advantage of null-steering is most obvious when taking the case of the tow-ship and two distinct sources within proximity of each other's conjugate angle in a high SNR environment (allowing more multiple target interference). All sources, including the tow-ship, are set at the same (0dB) source level. The tow-ship, in this case about 60-100 times closer than the rest of the sources, appears significantly louder. In the cardioid case, the inherent resolution issue forward of the beam is most apparent, especially when the sources are caught, as is the case for sources 1 and 4 (45°,-50°), in the sidelobes of the near-field tow-ship. This is less of an issue for sources 2 and 5 (100°,-105°), which appear distinctly, yet the tow ship still dominates the acoustic field, as shown in the Figure 40 below on a color dB for signal recognition, and a polar dB plot for illustration of the near field effect sidelobe structure.

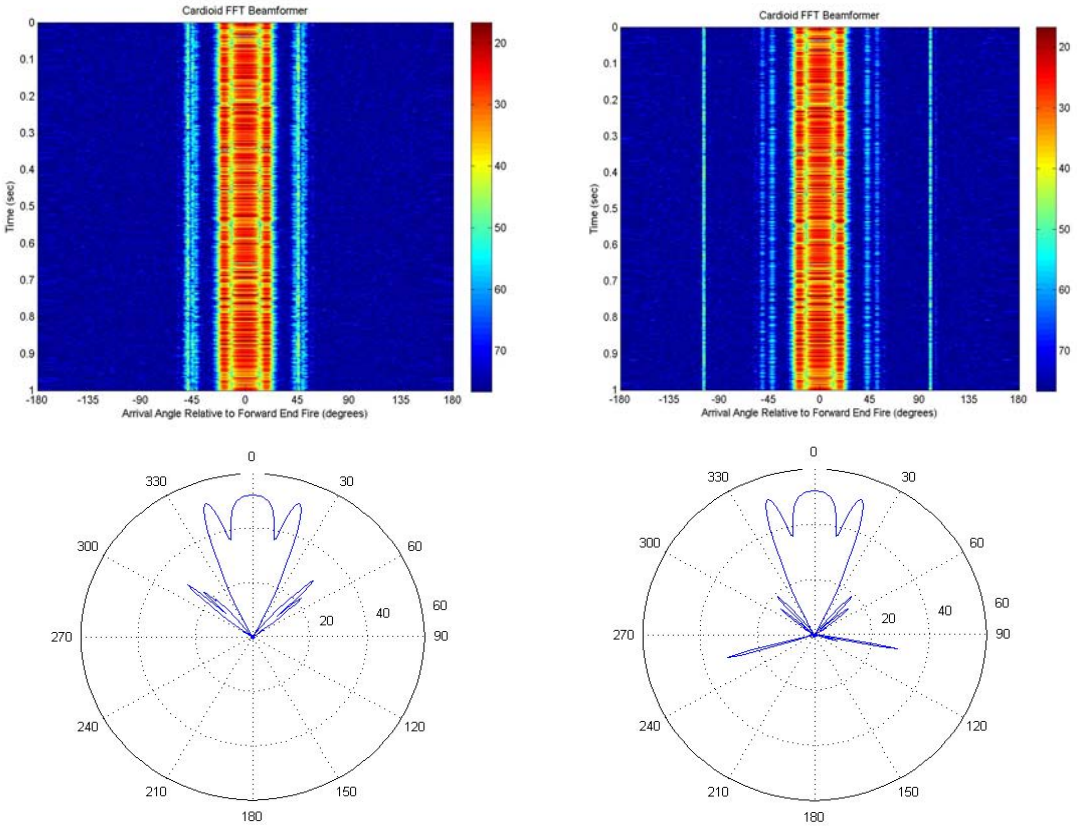

Figure 40. Left: Cardioid Sources 1&4 (45°,-50°) with Tow-Ship (0°) Right: Cardioid Sources 3&5 (100°,-105°) with Tow-Ship (0°)

With cardynull processing, the dynamic null-steering element will significantly nullify the effects of endfire targets (in which the conjugate angle is also the look angle), thus "flattening" the mainlobe of the tow-ship, and allowing the off-broadside targets to appear more distinct and with a higher dB gain relative to the tow-ship in Figure 41.

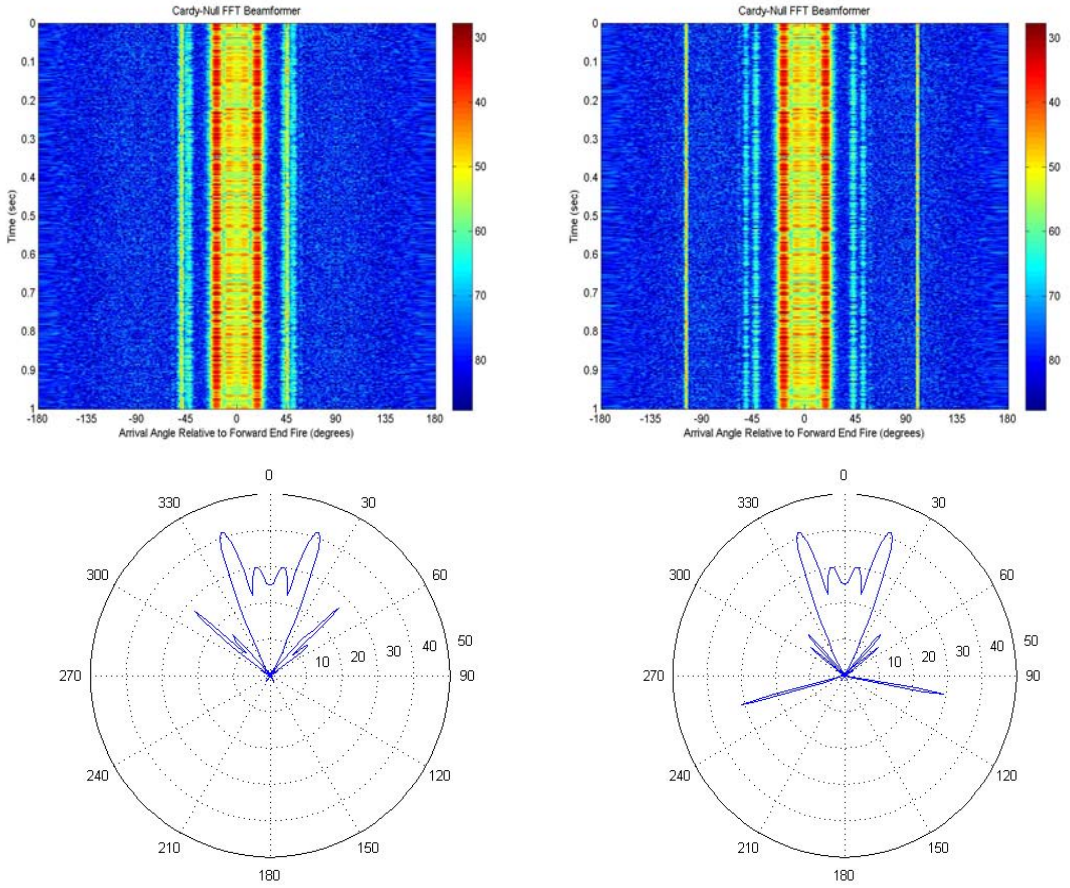

Figure 41. Left: Cardynull Sources 1&4 (45°,-50°) with Tow-Ship (0°). Right: Cardynull Sources 3&5 (100°,-105°) with Tow-Ship (0°)

When full dynamic null-steering is implemented, the tow-ship mainlobe is completely suppressed by null placement at endfire. In addition, side lobes are now also degraded in intensity such that sources previously hidden are more clearly visible, as well as at a much higher dB gain relative to the tow-ship in Figure 42. The benefits of dynamic null-steering in this case are still just as pronounced in the low SNR environment, as illustrated in Figures 43-44, with the addition of noise "washout" of the conjugate source angles and sidelobe structure of the towship.

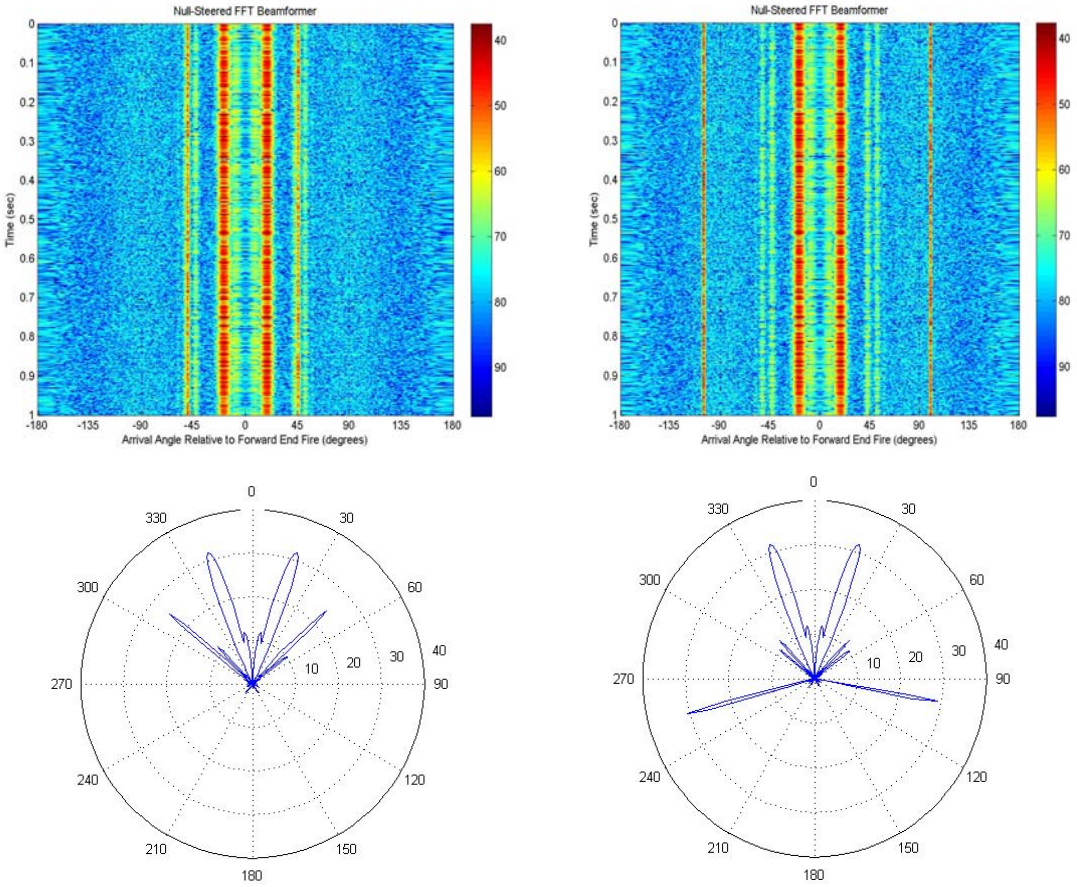

Figure 42. Left: Null-Steered Sources 1&4 (45°,-50°) with Tow-Ship (0°). Right: Null-Steered Sources 3&5 (100°,-105°) with Tow-Ship (0°)

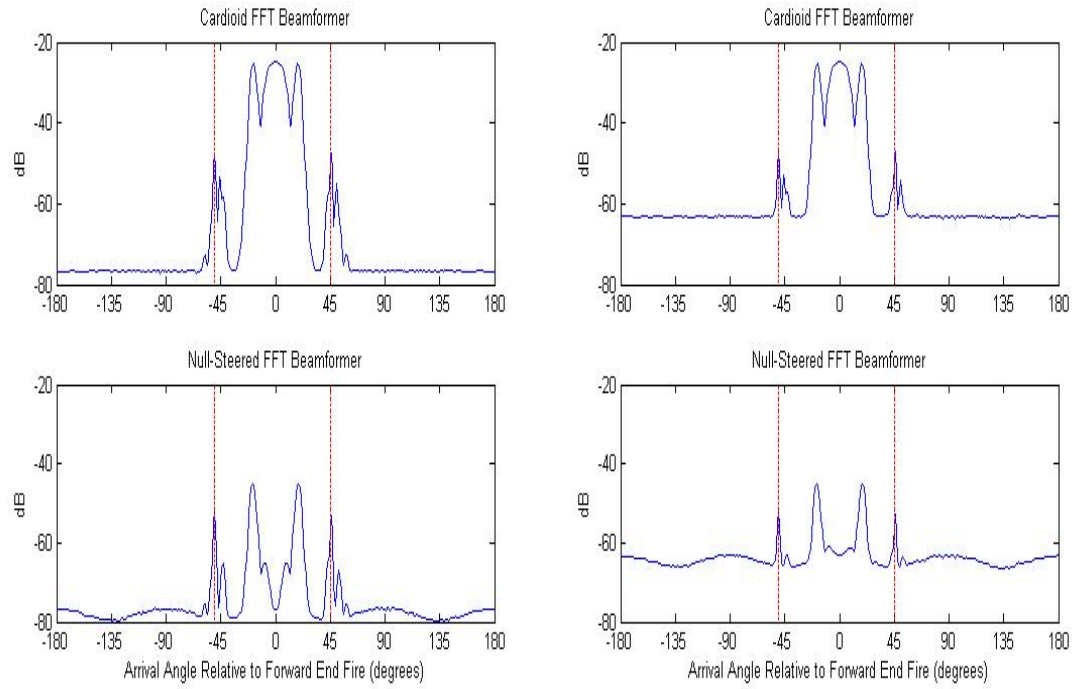

Figure 43. Null-Steered Sources 1&4 (45°,-50°) with Tow-Ship (0°) for Both Noiseless (Left) and Noisy (Right) Environments

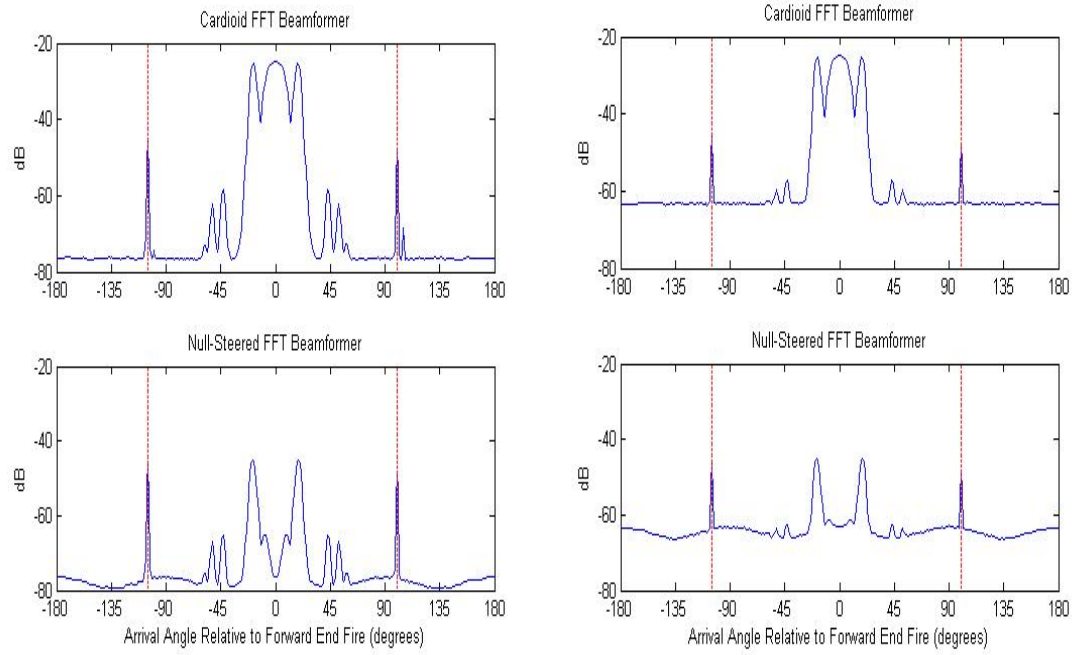

Figure 44. Null-Steered Sources 3&5 (100°,-105°) with Tow-Ship (0°) for Both Noiseless (Left) and Noisy (Right) Environments

The final case for the benefits of null-steering utilize the combination of a noisy interferer (Source 2) and the sidelobes of the near-field tow-ship "blinding" out a hidden Source 1 using standard cardioid processing, which becomes increasingly more apparent after dynamic null-steering as demonstrated in Figure 45.

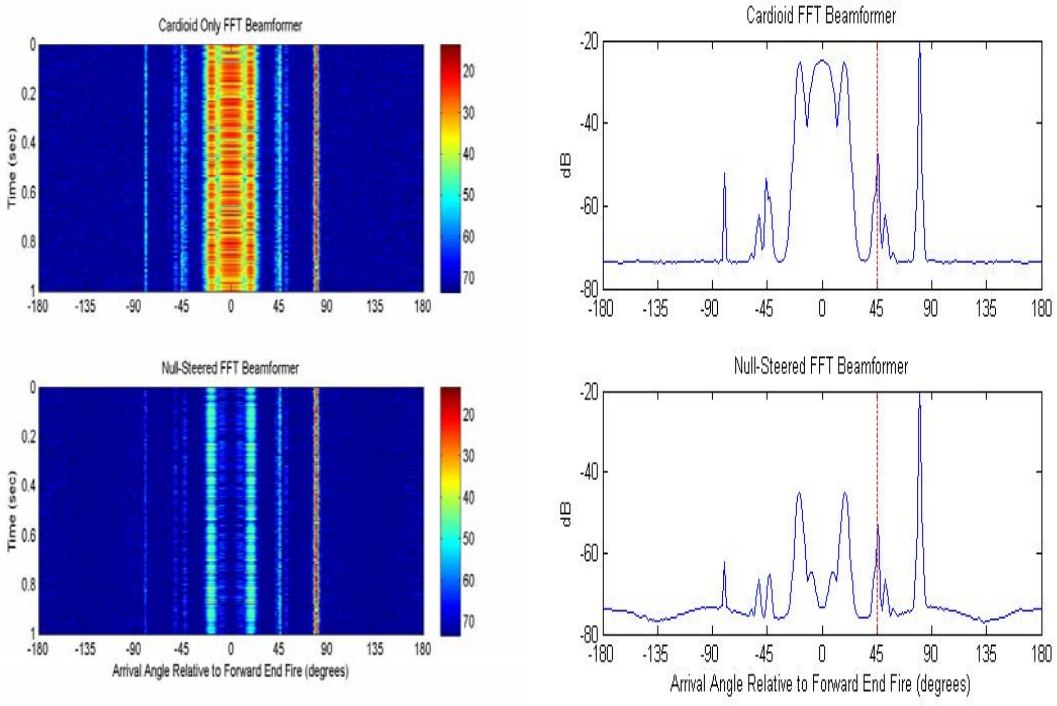

Figure 45. Cardioid and Null-Steered Comparison of Source 1 (45°) and Loud Interferer (80°) with Tow-Ship (0°)

The effects are even more pronounced in the low SNR environment of Figure 46 below, where both the effects of the near-field of the tow-ship and the ambiguous arrival of the loud interferer are washed out. In this case, the loud interferer itself dominates the acoustic field and the background noise, although set at the 0dB SNR level, has less detriment to signal recognition.

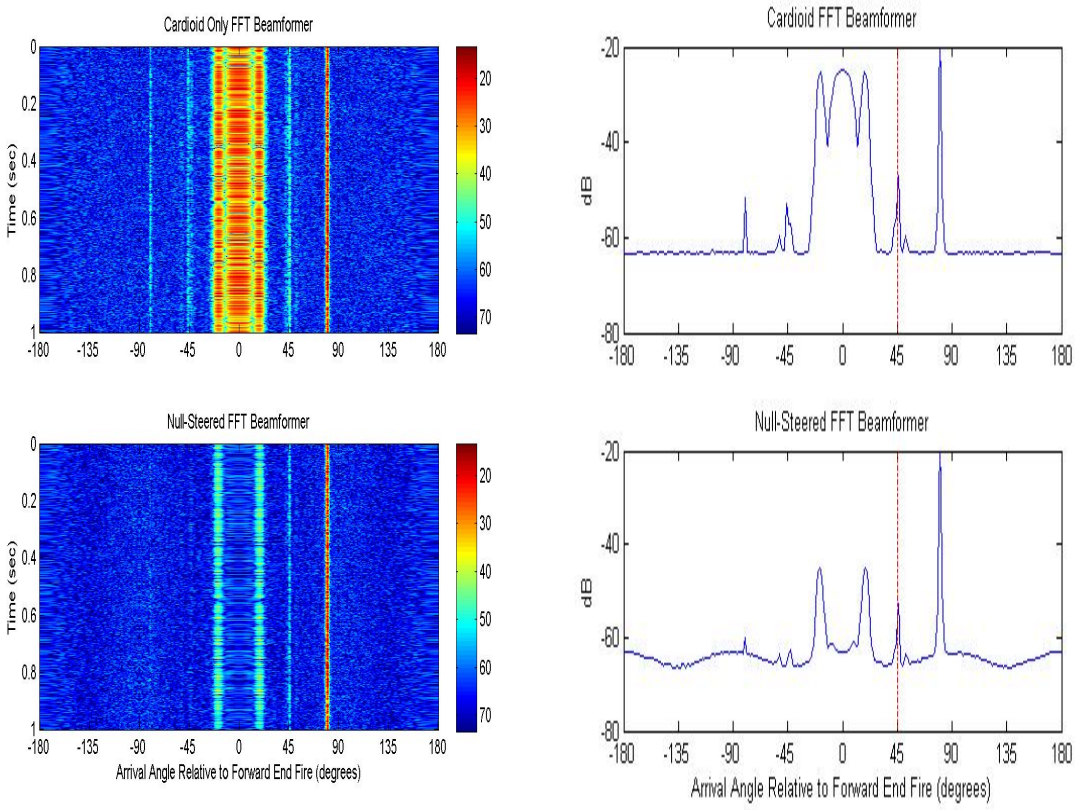

Figure 46. Cardioid and Null-Steered Comparison of Source 1 (45°) and Loud Interferer (80°) with Tow-Ship (0°) in Noisy Environment

THIS PAGE INTENTIONALLY LEFT BLANK

VI. CONCLUSIONS

The benefits of vector sensor arrays over their scalar pressure counterparts have been demonstrated with conventional linear cardioid processing, both in directivity gain and ambiguity rejection, due to the addition of three more sensor channels.[7] Yet the flexibility inherent in these channel weightings has also demonstrated processing schemes which may provide additional benefits over conventional linear cardioid processing. These processors can be utilized with established FFT algorithms to sufficiently approximate the ideal correlation processor, sacrificing accuracy for efficiency of processing time, and remain much easier to implement than other computationally intensive, directivity maximizing techniques such as data adaptive processors.

In this thesis, we have analyzed the benefits of various linear and nonlinear "hybrid" beamforming processors available with vector sensor processing, and compared them, using directivity, SNR gain and ambiguity rejection as a standard metric, against test cases developed in the previous work of Jautaikis [7]. The analysis shows that although higher directivity gain in the look direction is achieved in both low and high noise environments by the uniformly weighted linear cardioid, the dynamic null-steered processor provides unquestionable ambiguity rejection benefits in the same environments for all look angles (though with the sacrifice of directivity) providing added benefit in the presence of noisy interferers. A nonlinear hybrid of the two processors, the cardynull, provides a combination of the benefits of the two in most cases.

The inherent advantage of incorporating these processors in FFT beamforming allows for a reasonable real-time processing window for the data, such that one processor can be utilized in first acquiring low SNR targets of interest in tactical ocean environments, then another processor (or a varying degree nonlinear combination of the two) can then be used for better ambiguity resolution without the need for target motion analysis or lengthy post-processing times.

THIS PAGE INTENTIONALLY LEFT BLANK

LIST OF REFERENCES

[1] G. L. D'Spain, W. S. Hodgkiss, G. L. Edmonds, J. C. Nickles, F.H. Fisher, and R. A. Harriss, "A Vertical Array of Directional Acoustic Sensors," IEEE Proceedings of OCEANS '92, pp 340-345 (1992).

[2] G. L. D'Spain, W. S. Hodgkiss, G. L. Edmonds, J. C. Nickles, F.H. Fisher, and R. A. Harriss, "Initial Analysis of the Data from the Vertical DIFAR Array," IEEE Proceedings of OCEANS '92, pp 346-351, (1992).

[3] H. Cox, R.M. Zeskind, "Adaptive Cardioid Processing," IEEE Proc. of 26th Asilomar Conf., pp 1058-1061 (1992).

[4] B. A. Cray, A. H. Nuttall, "Directivity Factors for Linear Arrays of Velocity Sensors," J. Acoust. Soc. Am., 110, pp. 324-331 (2001).

[5] A. Nehorai, E. Paldi, "Acoustic Vector Sensor Array Processing," IEEE Trans. Sig. Proc. 42, pp 2481-2491 (1994).

[6] K. B. Smith, and A.V. van Leijen, "Steering Vector Sensor Array Elements with Cardioids, Hippopedes, and other Beam Shapes," J. Acoust. Soc. Am. 122, 370-377 (2007).

[7] E. P. Jautaikis, "Linear and Adaptive Plane Wave Beamforming with Towed Array of Acoustic Vector Sensors," NPS Thesis, M.S. Engineering Acoustics (2007).

[8] K. B. Smith, E. P. Jautaikis, S. T. Psaras, J. DiBiase, R. Barton "Performance Comparison Between Various Processing Techniques for Vector Sensor Line Arrays," 2007 Joint Undersea Warfare Technology Fall Conference. Groton, CT.

[9] A. B. Coppens, A. R. Frey, L. E. Kinsler, and J. V. Sanders, "Fundamentals of Acoustics," John Wiley and Sons, Inc., 2000.

[10] F. B. Jensen, W. A. Kuperman, M. B. Porter and H. Schmidt, "Computational Ocean Acoustics," AIP Press, 2000.

[11] K. B. Smith and F. D. Tappert, "UMPE: The University of Miami Parabolic Equation Model, Version 1.0," Marine Physical Laboratory Technical Memo 432, 1993.

[12] K. B. Smith, "Convergence, Stability, and Variability of Shallow Water Acoustic Predictions using a Split-Step Fourier Parabolic Equation Model," J. Comp. Acoust., pp 243-285 (2001).

[13] L.J. Ziomeck, “Fundamentals of Acoustic Field Theory and Space-Time Signal Processing,” CRC Press , 1995.

[14] D. J. Defatta, W. S. Hodgkiss, and J. G. Lucas, “Digital Signal Processing: A System Design Approach,” John Wiley and Sons, Inc., 1988.

[15] Thomson, D. J. and Chapman, N. R., “A wide-angle split-step algorithm for the parabolic equation,” J. Acoust. Soc. Am. 74, pp. 1848-1854 (1983).

INITIAL DISTRIBUTION LIST

1. Defense Technical Information Center
   Ft. Belvoir, VA

2. Dudley Knox Library
   Naval Postgraduate School
   Monterey, CA

3. Prof. Kevin B. Smith
   Naval Postgraduate School
   Monterey, CA

4. Dr. Joseph DiBiase
   NUWCDIVNPT
   Newport, RI

5. Dr. Ellen Livingston
   ONR, 321OA
   Arlington, VA

6. Dr. Mike Traweek
   ONR, 321MS
   Arlington, VA

7. Dr. John Tague
   ONR, 321SS
   Arlington, VA

8. NAVSEA 05
   NAVSEA
   Washington, DC

9. NAVSEA 06
   NAVSEA
   Washington, DC

10. Dave Yoshihara
    Director, N00ASW
    COMPACFLT
    Pearl Harbor, HI

11. Dick Corpus
Deputy N7
Fleet ASW Command
San Diego, CA

12. PEO IWS5a
Chhay Lim
Washington, DC

13. PEO SUBS
Washington, DC

14. SUBDEVRON 12
Groton, CT

15. COMNAVSURFOR
San Diego, CA

16. COMVANSUBFOR
Norfolk, VA

17. COMSUBPAC
Pearl Harbor, HI

18. COMUNDERSEASURV
Dam Neck, VA